

CMB POLARIZATION AT LARGE ANGULAR SCALES: DATA ANALYSIS OF THE POLAR EXPERIMENT

CHRISTOPHER W. O'DELL¹, BRIAN G. KEATING², ANGELICA DE OLIVEIRA-COSTA³, MAX TEGMARK³, AND PETER T. TIMBIE

Department of Physics, 2531 Sterling Hall, University of Wisconsin – Madison, Madison, WI 53706

Draft version, February 7, 2020

ABSTRACT

The coming flood of CMB polarization experiments, spurred by the recent detection of CMB polarization by DASI, will be confronted by many new analysis tasks specific to polarization. For the analysis of CMB polarization data sets, the devil is truly in the details. With this in mind, we present the details of the data analysis for the POLAR experiment, which recently led to the tightest upper limit on the polarization of the Cosmic Microwave Background Radiation at large angular scales. We discuss the data selection process, mapmaking algorithms, offset removal, and the likelihood analysis which were used to find upper limits on the polarization. We also discuss simulations used to test our analysis techniques and to probe the fundamental limitations of the experiment.

Subject headings: cosmic microwave background: – cosmology: observations, polarization, mapmaking

1. INTRODUCTION

The detection of polarization in the Cosmic Microwave Background (CMB) has been a long sought goal for cosmology. CMB polarization was recently detected at sub-degree angular scales by the DASI instrument, a ground-based interferometer (Kovac et al. 2002). While information in the CMB polarization at degree and sub-degree angular scales further confirms the standard cosmological model, polarization information at larger angular scales has the potential to provide additional information regarding the formation and evolution of the universe. The process of reionization leaves a characteristic signature on CMB polarization at large angular scales which can be used as a means to determine the epoch of reionization (Zaldarriaga 1997; Hu 2000; Kaplinghat et al. 2002). The power spectrum of CMB polarization at angular scales greater than a degree or so is sensitive to inflationary model parameters such as the inflaton potential and the energy scale of inflation, as well as primordial gravitational waves (Kamionkowski & Kosowsky 1999; Kinney 1998; Knox & Song 2002; Turner & White 1996).

These exciting rewards, taken together with increasingly sensitive receiver technologies, have set the stage for a host of new CMB polarization experiments. These experiments will be faced with new and more challenging analysis tasks than for the simpler case of anisotropy, and it is with that in mind that we now set out to report the details of the data analysis of the POLAR experiment.

POLAR (Polarization Observations of Large Angular Regions) was designed to measure the polarization of the CMB on large angular scales, in the K_a frequency band from 26 – 36 GHz. This HEMT-based correlation polarimeter operated for a single season in the Spring of 2000 near Madison, Wisconsin. The data from this single season led to simultaneous upper limits on E and B-type CMB

polarization of $T_E, T_B < 10 \mu\text{K}$ at 95% confidence, results which were initially presented in Keating et al. (2001) (hereafter K01). The details of the POLAR instrument and its operation were later described in Keating et al. (2002) (hereafter K02). In this paper we fully discuss the details of the data selection and analysis techniques used to arrive at the results in K01. We also discuss the results of a recent cross-correlation analysis of the POLAR data with anisotropy data from the COBE-DMR experiment, presented fully in de Oliveira-Costa et al. (2002).

The rest of this paper is organized as follows. We review the basic properties of the POLAR instrument in §2. In §3, we discuss the data selection procedures that were used to remove large amounts of contaminated data. §4 describes the mapmaking algorithms used to transform the raw data into sky maps of Q and U , and provides a full pipeline simulation in order to test the algorithms. §5 presents the likelihood analysis used to arrive at the upper limits on CMB polarization, as well as the evaluation of the polarization power spectra and some commentary on the lack of substantial foreground contamination. Finally, in §6, we discuss the limitations of our experiment that could be improved upon in future projects.

2. INSTRUMENT

POLAR observed the local zenith from the University of Wisconsin – Madison's Pine Bluff Observatory in Pine Bluff, Wisconsin (Latitude $+43^\circ 01'$, Longitude $+89^\circ 45'$) using a simple drift-scan strategy, with a 7° FWHM beam defined by a K_a -band microwave feed horn. A correlation radiometer operated as a polarimeter that was instantaneously sensitive to the U Stokes parameter. The full RF band was divided into 3 sub-bands, 32–36 GHz, 29–32 GHz, and 26–29 GHz. Each of the channels was detected by a separate microwave correlator, labelled J1, J2, and J3, respectively. The constant rotation of the instrument about its vertical axis allowed for simultaneous detection of both the Q and U Stokes parameters.

POLAR employed a phase-sensitive detection technique. The relative phase of the two arms of the correlation radiometer was modulated at approximately 1 kHz. A simple analog lock-in circuit produced the actual “in-phase”

¹ Currently at the Department of Astronomy, University of Massachusetts, Amherst, MA 01003

² Division of Physics, Math, and Astronomy, California Institute of Technology, Pasadena, CA 91125; bgk@astro.caltech.edu.

³ Department of Physics, University of Pennsylvania, Philadelphia, PA 19104

polarization signal. However, the instrument simultaneously locked into the chop frequency shifted by $\frac{\pi}{2}$, yielding pure noise. We obtained one of these “quadrature-phase channels” (QPC) for each of the three in-phase channels (IPC). The quadrature-phase channels were a good monitor of the noise in our system, and as such were employed in several places throughout the analysis pipeline. We will use the terms J1i, J2i, and J3i to refer to the three in-phase channels, while J1q, J2q, and J3q refer to the corresponding quadrature-phase (noise) channels.

POLAR sampled all of its channels at 20 Hz, and employed 5 Hz, 24 dB/octave low-pass filters to prevent aliasing. The sampled data were continuously recorded to files, each containing precisely 9000 samples or 7.5 minutes of data; these files are one of the fundamental data units to be discussed throughout this paper. The instrument was calibrated daily with a 3-mil thick dielectric sheet. We did not calibrate the instrument when the weather was poor. The calibration was accurate to about 10%, based upon laboratory measurements of the dielectric sheet properties; see O’Dell et al. (2002) for details. Each *section* of data is defined as the longest period of observations between calibrations. Approximately fifty such sections were collected throughout the observing season, each some 2–24 hours in length.

POLAR’s constant rotation rate allows us to characterize its response to a polarized signal as follows:

$$\mathbf{y}(t) = I_0 + C \cos \omega t + S \sin \omega t + Q \cos 2\omega t + U \sin 2\omega t + n(t) \quad (1)$$

where $\omega = 2\pi f = 0.2055 \text{ rad s}^{-1}$ was the (angular) rotation frequency. The constant offset I_0 is due to coupling of the unpolarized total power signal into the polarization channels via the nonzero cross-polarization of the instrument. This offset term was typically 10-100 mK, depending on the channel; during good weather its stability was better than 0.6 mK per hour. C and S are signals modulated at the rotation frequency (referred to hereafter as 1ϕ signals), and can be caused by various types of ground pickup and other systematic effects. Via Equation (1), linearly polarized signals will produce a signal in the data stream at twice our rotation frequency, henceforth called the 2ϕ frequency.

3. OBSERVATIONS AND DATA SELECTION

During the observing season, POLAR observed 24 hours per day over a two month period, yielding roughly 750 hours of data. However, the observing season contained a large diversity of weather conditions, and this led to a correspondingly large diversity of data quality. Thus, developing robust data selection criteria was one of the most critical tasks in the data analysis pipeline. Because of the data’s diversity, we were not able to arrive at a single selection criterion; rather, we developed a battery of conditions that the data were required to meet before being accepted. Our underlying philosophy was to cut “more rather than less”, to ensure a final data set with the minimum level of systematic effects present.

Many effects can conspire to contaminate the Q and U signals, be they instrumental, atmospheric, or celestial. We wish to flag and remove any data with a non-cosmological contribution to our signal that mimics a cosmological signal in a way that we cannot account for and

remove. One such example occurs when observing through clouds with a slightly asymmetric beam; the (generally asymmetric) cloud will produce a 2ϕ signal via the instrumental cross-polarization, and will lead to an apparent polarization signal in Q and U . This effect cannot be modelled accurately enough to fully remove, so the data must be cut.

The rest of this section will describe the various criteria we established in order to robustly separate clean from contaminated data. There were three basic types of cuts used: instrument-based, celestial, and data-based. Instrument-based cuts were those in which our systems were not functioning properly or led to unanalyzable data; an example of this was jerky azimuthal rotation (which occasionally occurred during the season). Celestial cuts were those in which some non-cosmological celestial source was in a position to contaminate our data, such as the sun, moon, or galaxy. Data-based cuts were those which used noise properties of the data itself to assess contamination. Table 1 lists all of the cut criteria used in the POLAR-analysis; the entries in the table will be described in more detail throughout the rest of this section.

3.1. The Fiducial Data Unit

Before deciding those statistics upon which to cut, the question of the *time scale* over which to cut must be addressed. Cutting on longer segments ensures a good estimation of the noise properties of the data segment, but the noise may not be stationary over the entire segment. Shorter segments have the opposite problem - good stationarity but a poorer noise estimation. We chose to cut at the *file* level of the data, where a data file contained 7.5 minutes of data as described above. This segmenting was convenient (it is how our data were packaged already) and ensured good noise stationarity while allowing for a reasonable estimation of the low frequency noise (necessary for our mapmaking algorithms).

A related question to the cutting timescale is whether or not to cut all channels simultaneously versus separately. An important fact of our experiment was that some of the effects contaminating the data were frequency dependent;

TABLE 1
EFFECT OF VARIOUS DATA CUTS. SEE TEXT FOR DETAILS.

Cut Type	Hours ^a Surviving	Hours ^b Cut	Indiv. ^c Hours Cut
Full Data Set	746.5 (100%)	0 (0%)	0 (0%)
Instrument	629.3 (84.3%)	117.3 (15.7%)	117.3 (15.7%)
Celestial	270.9 (36.3%)	358.4 (48%)	434.3 (58.2%)
Data-based	152 (20.4%)	118.9 (15.9%)	478 (64%)
Length-based	78.1 (10.5%)	73.8 (9.9%)	N/A
ROD Cuts	71.1 (9.5%)	7 (0.9%)	N/A

^aThe amount of data left after that cut and all the cuts above it have been applied.

^bAmount of data cut at that stage.

^cAmount of data that would have been cut if that particular criterion were the only one applied.

in particular, channel J3 (26–29 GHz) often showed evidence of a spurious signal when the other two channels did not. For this reason, we opted to perform the data-based cuts on each of our three channels individually; the instrumental and celestial cuts had no strong frequency dependence, and hence were applied equally to the three channels.

3.2. Instrument-Based Cuts

As our system generally operated as expected throughout the entire season, we only had to perform two instrument-based cuts. The first cut was to remove any files during which the system wasn't rotating for the entire file, or the rotation was unnaturally slow or jittery. These primarily occurred at those times when data acquisition was initiated and system rotation began. It also occurred later in the season from wear on the rotation bearing. This cut removed 1.8% of the data.

The other instrument-based issue was dew formation on the optics, a common problem in ground-based experiments. Specifically, when the relative humidity was high for an hour or more, moisture condensed on the vacuum window. This immediately led to a spurious polarization signal in the data. The mechanism was likely that ambient radiation scattered off the layer of water, leading to the apparent signal. The dew problem didn't manifest itself until later in the season, when conditions became warmer and more humid. Of the 750 hours of recorded data, dew contaminated approximately 105 hours, or 14% of the total data set.

3.3. Celestial Cuts

Because the feedhorn accepts some radiation from all angles, a celestial source will contribute a nonzero amount of radiation when it is anywhere above the horizon. We must be concerned about celestial objects leaking some radiation through a sidelobe in our beam, or the main lobe if the source ever gets close enough to the local zenith. We must be concerned with the sun, moon, and planets, as well as point source and diffuse radiation from the galaxy.

3.3.1. Solar System Objects

Solar radiation is potentially the most troublesome of all celestial radiation sources. At microwave frequencies, the sun can be treated as roughly an 11,000 Kelvin blackbody with an angular width of 0.5° FWHM (Zirin et al. 1991). We can estimate the antenna temperature of any point-like source with brightness temperature T_B , as seen by an antenna with an azimuthally symmetric response $B(\theta)$, as

$$T_a = T_B B(\theta) \frac{\Omega_S}{\Omega_B} \quad (2)$$

where Ω_S is the solid angle of the source, Ω_B is the solid angle of the receiving antenna, and θ is the angle of the source from the antenna boresight. For POLAR, $\Omega_B \sim 0.0219$ sr, found by integrating $\Omega_B = \int_{4\pi} B(\vec{r}) d\vec{r}$ using the measured beam function. Conservatively assuming the sun is 1% polarized, we can use the POLAR beam profile to determine worst-case solar contamination as a function of the solar altitude. We require the solar altitude to be less than 70° ; using attenuation by the feedhorn alone, this yields a worst-case spurious polarization of $< 0.4 \mu K$.

However, POLAR also contained two ground screens (see K02 for details). A celestial object below 40° elevation must diffract over the inner ground screen to reach the feedhorn, which in practice will reduce the solar contamination to even lower levels. Applying this cut to our data removed a substantial 288 hours, or 39% of the total data set.

We can treat contamination by the moon in a similar fashion. The lunar model by Keihm (1983) shows that the moon can be treated as a blackbody of approximately 240 K (in its brightest phase), 0.5° angular diameter, and $\lesssim 1\%$ polarization. Using Equation (2) and the measured feedhorn beam pattern, and assuming 1% polarization, lunar emission falls below $1 \mu K$ at zenith angles greater than 22° , which coincidentally corresponds to the highest lunar elevation achieved during the season. To be conservative, however, we require the moon to be further than 40° from the beam center; this prevents the moon from shining directly on the feedhorn. Even without the inner ground screen, our model shows that lunar contamination will then be less than $0.05 \mu K$. Including the attenuation by the inner ground shield will reduce this level even further. The lunar cut removed an additional 28 hours of data beyond the solar cut.

In principle, contamination by the planets was also possible. Employing Equation (2), we have calculated the possible contamination effects of the planets. Table 2 shows the results of this calculation; it displays the maximum calculated total intensity as seen by POLAR taking into account both the distance to the source as well as the angle from our boresight. The sun and moon total intensity are also shown for comparison. The maximum planetary signal is seen to be from Jupiter, and was estimated to be $\sim 0.01 \mu K$. Including the fraction of the source that is polarized will reduce this number even further. Thus in the case of POLAR, planetary radiation can be safely neglected.

3.3.2. Galactic Foreground Emission

Finally there is the question of emission from the galaxy, either from diffuse or point sources. POLAR has a sen-

TABLE 2
SOLAR, LUNAR, AND PLANETARY PARAMETERS
DURING THE POLAR OBSERVING SEASON.

Planet	$T_B[K]^a$	Max Elevation	Signal [μK] ^b
Sun	11,000	68.7°	6500
Moon	240	67.8°	69
Mercury	190	72.6°	0.0053
Venus	470	67.7°	0.0038
Mars	190	70.5°	0.0011
Jupiter	150	64.6°	0.011
Saturn	150	63.4°	0.0016

^aDisk-Averaged brightness temperature near 30 GHz, as based on Keihm (1983); Zirin et al. (1991); Greve et al. (1994).

^bMaximum antenna temperature of source in total intensity.

sitivity to point sources of roughly $2 \mu\text{K}/\text{Jy}$. Using the WOMBAT point-source catalog for 30 GHz (Sokasian et al. 2001), we calculate that there are approximately 40 sources that passed through our beam contributing greater than $1 \mu\text{K}$ antenna temperature in intensity. Only three sources contribute greater than $10 \mu\text{K}$. We chose not to perform a point-source based cut as detecting these sources, while challenging, would be both interesting and relatively easy to identify as galactic versus cosmological in origin.

The observations described were conducted over a wide range of galactic latitudes and therefore there is a potential for diffuse galactic contamination, especially at low latitudes (Bennett et al. 1996; Davies et al. 1996). Galactic synchrotron emission can be up to 70% polarized (Rybicki & Lightman 1979). No maps of polarized synchrotron emission exist at 30 GHz, and extrapolation of measurements at lower frequencies, *e.g.* Brouw & Spoelstra (1976), is not a reliable probe of synchrotron polarization at 30 GHz due to Faraday rotation. Although the unpolarized intensity is apparently not correlated with the polarized intensity as shown in de Oliveira-Costa et al. (2002), we attempt to limit our susceptibility to synchrotron emission by only using data corresponding to Galactic latitudes $|b| > 25^\circ$.

3.4. Data-Based Cuts

Together, the instrument-based and celestial cuts removed approximately 64% of the original 750-hour data set. cursory analysis, however, immediately revealed that spurious signals still remained in this preliminary (post-cut) data set at sometimes high levels. This is not surprising given that the weather in Wisconsin is highly variable in the spring, and much of the loading on our system was due to atmospheric emission. Especially important was the presence of clouds, which as already noted can easily mimic a polarized signal. Unfortunately, we were unsuccessful in developing a good cloud monitor. Data containing some cloud cover information is available from both the National Weather Service (NWS) and the GOES-8 satellite, as described in K02. We found that neither correlated particularly well with periods of bad data. The NWS data were taken from the Dane County Regional Airport, roughly 35 km from our site. The GOES data were in the form of fields 5 km x 5 km wide, but typically the closest such field was about 20 km from our site. As cloud cover varies substantially over these distances, the cloud cover data were of little use as a cut statistic. Thus we follow the standard practice of deriving selection statistics that are based on characteristics of the data itself in order to serve as a measure of the quality of observing conditions.

3.4.1. The 1ϕ Cut

The initial statistic that was obviously correlated with spurious polarization signals was a high 1ϕ signal, *i.e.* signals with a high C and S as defined in Equation (1). Signals modulated only at the 2ϕ frequency correspond to true polarization signals; thus, a signal that has harmonics at both 1ϕ and 2ϕ cannot correspond to a true celestial signal. This is most easily seen in the power spectrum of the data. As an example, consider Figure 1. The left-hand (a) panel shows a classic, roughly featureless power spectrum with almost no $1/f$ noise, taken during a period of

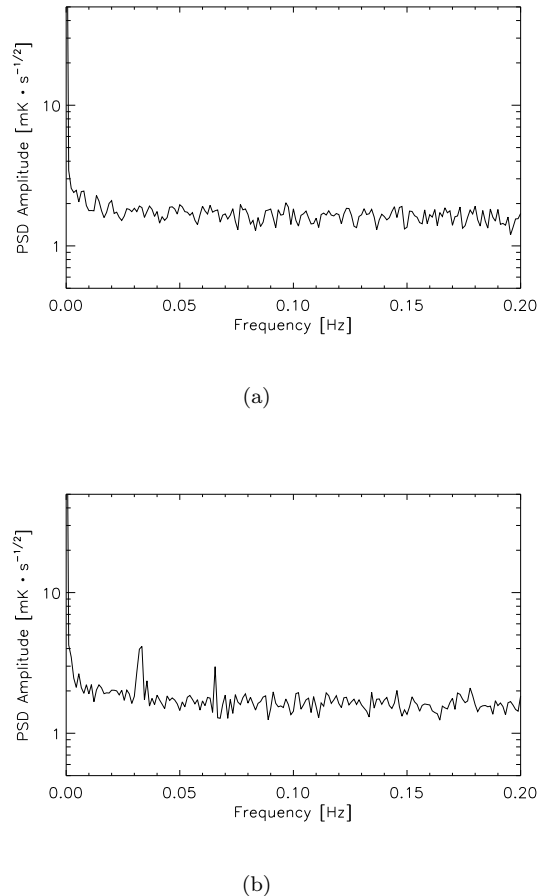


FIG. 1.— Low frequency power spectrum of two sections of data for channel J2i. Panel (a) shows a power spectrum of the time stream when the weather is good and systematic effects are low. Panel (b) displays a similar period when clouds appeared; there is a dramatic appearance of spikes at both the 1ϕ and 2ϕ frequencies. This motivated our using the strength of the 1ϕ peak as a cut statistic. True celestial polarization signals will appear at the 2ϕ frequency only.

good weather for channel J2i. But as the weather worsens, due to clouds and/or increased humidity and water vapor, features at the 1ϕ and 2ϕ frequencies appear, as shown in Figure 1(b). This motivates a study of the correlation between 1ϕ and 2ϕ signals in the time stream.

The 1ϕ values for each data file were computed from the mean $\sqrt{C^2 + S^2}$ statistics for each data file, and the 2ϕ statistics were computed similarly. However, because the noise floor varied over time (due to atmospheric loading changes, gain drifts, etc.), a more useful statistic was the 1ϕ power relative to the noise floor, defined to be the mean power spectrum value between 3.0 and 5.0 Hz (this is well beyond the $1/f$ knee and any rotational harmonics, but before the anti-aliasing filter's roll-off frequency). We called these relative statistics the $1\phi_r$ and $2\phi_r$ statistics. Figure 2 displays these data plotted against each other for channel J2i, with both instrument-based and celestial cuts applied. The high degree of correlation between the two quantities is striking; this strongly motivated the use of the 1ϕ level as a cut statistic.

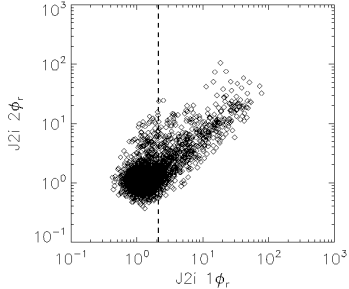


FIG. 2.— $2\phi_r$ vs $1\phi_r$ for the data channel J2i. Periods contaminated by sun, moon, and dew have been removed. The vertical dashed line shows the $1\phi_r < 2.1$ cut level.

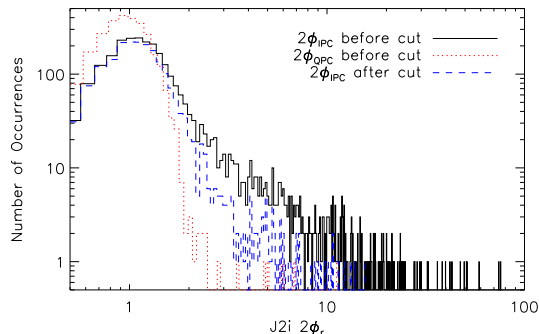


FIG. 3.— Histogram of $2\phi_r$ data for channel J2i. The solid (black) line represents all the data, with sun, moon, and dew-contaminated data removed. The dotted (red) line is the same data set for the QPC channel J2q; it can be thought of as the ideal $2\phi_r$ distribution for white noise. The dashed (blue) line is the $2\phi_r$ data after the $1\phi_r < 2.1$ cut was applied. Notice that a large fraction of the tail of the distribution has been removed, but a small portion still remains.

In order to determine a logical $1\phi_r$ cut level, we compared our data to the behavior of white noise. Monte-Carlos of Gaussian white noise show that this statistic should ideally be 1.0 ± 0.27 , distributed roughly as a Gaussian itself. We opted to cut whenever $1\phi_r > 2.1$; this is more than 4σ from the mean for white noise. Implementing this requirement, an additional 109 hours, or about 15% of the total data was cut. Figure 3 shows the effect of this cut on the data. It displays a histogram of the $2\phi_r$ level for channel J2i before and after the cut, as well as the same histogram for J2q (the corresponding noise channel). It is apparent from Figure 2 that there will still be some residual data points with high $2\phi_r$, regardless of the $1\phi_r$ cut. This motivated us to examine additional statistics that may also be correlated with the 2ϕ level, and therefore may serve as useful data selection criteria.

3.4.2. The Zeta Cut

It is well-known that the autocorrelation function and power spectrum of any data set form a Fourier transform pair, and hence the information in one is the same as the information in the other. For instance, a rise in $1/f$ noise leads directly to a higher “floor” in the autocorrelation function. Any signal in the data will also lead to a non-trivial autocorrelation function. We used that fact to our

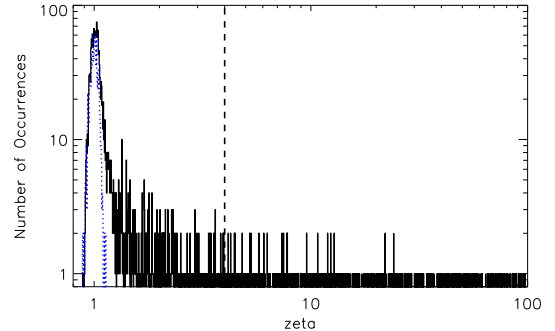


FIG. 4.— Distribution of the ζ Variable. The solid (black) curve shows the distribution of ζ for channel J2, with the basic sun, moon, and dew cuts applied. The dotted (blue) curve shows the ζ -distribution for simulated white noise run through our anti-aliasing filter. The vertical dashed curve is the cut level of $\zeta=4.0$.

advantage and defined the following statistic for each data file:

$$\zeta \equiv \frac{\sum_{lag=1}^{1000} C(y_{in})^2}{\sum_{lag=1}^{1000} C(y_{quad})^2} \quad (3)$$

where y_{in} denotes data from an in-phase channel and y_{quad} denotes data from the corresponding quadrature-phase channel. Simulations we performed show that a reasonable astrophysical signal (of, say, less than $100 \mu\text{K rms}$), would have a negligible contribution to ζ for POLAR. Equation (3) has an intuitive explanation; it is roughly the integral of the power spectrum between 0.01 Hz (near our lowest observable frequency) and 10 Hz (our Nyquist frequency), weighted by $1/f$, so low-frequency drifts cause ζ to increase rapidly. As such drifts are generally indicative of poor atmospheric conditions, ζ proves to be a sensible cut statistic.

Figure 4 shows a histogram of ζ values throughout the season (with the basic sun, moon, and dew cuts applied). Also shown in the plot is a model of our data stream with no $1/f$ noise or signal of any kind. As can be seen, this distribution is sharply peaked around 1.0, with more than 99.9% of the data lying below 1.2. However, any deviation from pure white noise will rapidly change the ζ value of the data. We found that requiring $\zeta < 4$ cut a small amount of data (about 3%) over the other cuts. Monte-carlos of the time stream showed that a reasonable celestial signal ($\text{rms} \sim 100 \mu\text{K}$) would never cause ζ to rise above the level of 1.4. Varying the actual cut level between $\zeta < 2$ and $\zeta < 5$ had very little effect on the final results.

3.4.3. Outliers in the Time-Ordered Data

Occasionally, birds, planes, electrical noise, etc., would cause short-lived yet large spikes in the data stream. For each data file and channel, we calculated the mean and standard deviation, and recorded how many standard deviations the first, second, and third strongest outliers were from the mean. We cut any data file whose *second largest outlier* was more than 5σ from the mean of that data. Data files with one strong outlier only rarely occurred, because our 5 Hz filters in conjunction with our 20 Hz data acquisition frequency guaranteed that even a delta-

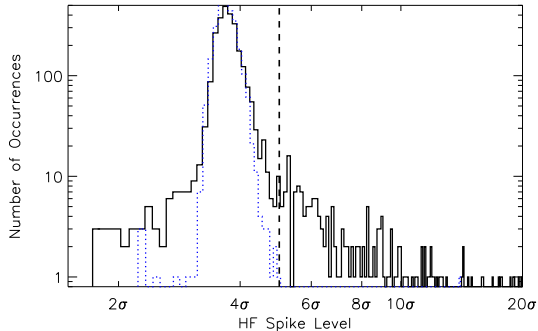


FIG. 5.— The distribution of second-worst outliers for each data file. Nominal sun, moon, and dew cuts have been applied. The solid (black) curve is the J2i channel, while the dotted (blue) curve is the J2q channel. The J2i channel has large wings on both sides of the main distribution, representing non-Gaussian behavior. The J2q behavior is strictly Gaussian. The vertical dashed line shows the applied cut level of 5σ .

function signal should have a width of at least a few samples in the data stream; thus the second strongest outlier proved a more robust indicator for such spurious effects. Their distribution is shown in Figure 5. This cut was useful, but highly overlapped with both the 1ϕ cut and the ζ cut. This cut removed $\sim 1.2\%$ of the data, or about 9 hours, in addition to all previous cuts.

3.5. Duration-Based Cuts

The next three selection criteria were based upon the length of surviving data segments. First, we required that if a data file were to survive, both its neighbors had to survive as well. Thus, if a segment of 10 files survived, the first and last of these would be cut. This was to ensure that the bad weather had truly ended, thus providing a nice 7.5-minute buffer. Secondly, we required a minimum of eight consecutive data files (one hour of data) to survive in order to keep any piece of data. This was to make sure we didn’t get into a situation where we only kept very short segments of data which statistically just happened to survive the cuts, even though perhaps they were part of a larger section of poor data.

Lastly, we required a minimum of three hours total to survive in a *section*⁴ of data for any data in that section to be retained; in contrast to the cut above, this three hours was not required to be contiguous. This cut was instituted primarily because the offset removal step of the analysis pipeline, described in §4.4. This algorithm takes place on a per-section basis, and effectively removes all information from very short sections of data; in the end we found it simpler just to remove these short sections of data. Table 1 shows the sizeable effect of the duration-based cuts; together, they removed more than 10% of the full data set.

3.6. Stokes Parameter Data Cuts

After we had applied these cuts to the entire data set, we were left with a set of “clean” data files for each channel and section. The cuts for a given quadrature-phase

⁴ A section of data is a data segment that was taken without interruption (this was typically about one day of data).

channel were the same as for the corresponding in-phase channel. The mapmaking techniques described in the next section enabled us to determine a mean Q and U for each channel and file, information we use to form additional cut criteria.

For each section and channel of data passing the cuts, we found that the distribution of Q and U for most sections was in general quite Gaussian, and appeared indistinguishable from white noise. Some sections, however, had a few strong outliers that survived into the $\{Q, U\}$ data set. We chose to proceed as in the time-ordered data case; for any section and channel with surviving data, we found the mean and standard deviation for the 2ϕ signal, *i.e.* $\sqrt{Q^2 + U^2}$. If this quantity was more than three standard deviations from the mean for that section, it was removed. Notice that this cut is not independent of the other cuts; it requires a fairly clean segment of data to get meaningful, clean distributions of Q and U in the first place. However, after instituting all the other cuts, this requirement only removed an additional 0.1% of the data (less than 1 hour).

4. FROM DATA TO MAPS

Now that we have our cleaned data set, our goals are clear: extract as much astrophysical and cosmological information from the data as possible. We seek to obtain both Q and U maps of the data set (for all channels), as well as bounds on CMB polarization at large angular scales. It is possible to reduce a large astrophysical data set to a map of the sky with no loss of cosmological information (Tegmark 1997a). This perhaps surprising result lets us kill two birds with one stone: we can make maps for visualization and comparison, and we can greatly compress our data set (roughly 16,000,000 \rightarrow 100 numbers) to make extracting cosmology from it more numerically tractable. In this section, we describe the algorithms that transform the POLAR data into map form. §5 discusses the cosmological implications of these maps.

4.1. The General Mapmaking Problem

The mapmaking problem is loosely defined as binning a data set into a pixelized map with minimum loss of cosmological information. Many authors have written on the mapmaking problem and all the nuances that can arise during its solution: Tegmark (1997a), hereafter T97a; Bond, Jaffe, Knox (1998), hereafter BJK; and Stompor et al. (2001), hereafter S01. Throughout the next sections, the mathematics of mapmaking will be discussed in great detail. Whenever discussing a vector, we use a lowercase boldface letter (*e.g.*, \mathbf{y}) to represent it. Similarly, matrices are represented by uppercase boldface letters (*e.g.*, \mathbf{W}).

The mapmaking problem proceeds as described in T97a. In general, a time ordered data vector $\mathbf{y} = \{y_1, \dots, y_{n_t}\}$, where n_t is the number of samples, can be written as a sum of signal plus noise. If the signal derives from an underlying map on the sky $\mathbf{x} = \{x_1, \dots, x_m\}$ with m pixels, then one can write

$$\mathbf{y} = \mathbf{A}\mathbf{x} + \mathbf{n} \quad (4)$$

where \mathbf{n} represents the system noise, and \mathbf{A} is called the “pointing matrix” and describes how to transform the data from “data space” to “map space”. The pointing matrix

is described in more detail in §4.2.1. In general, we can let the underlying map \mathbf{x} include the beam smoothing, or we can let the pointing matrix \mathbf{A} encode the beam pattern in addition to the scan strategy. Throughout this work, we make the first choice (which is generally simpler to implement).

The noise vector \mathbf{n} is characterized by the *timestream noise covariance matrix*, $\mathbf{N} \equiv \langle \mathbf{nn}^t \rangle$, where we assume that $\langle \mathbf{n} \rangle = 0$ without loss of generality. For white noise, the noise covariance matrix will reduce to a multiple of the identity matrix. More complicated noise will in general *correlate* different measurements y_i with each other (for instance, in the presence of $1/f$ noise). It is assumed that the instrumental noise is uncorrelated with the signal. §4.2 describes how the noise was estimated from the time stream for POLAR.

Given the pointing matrix \mathbf{A} and the noise statistics \mathbf{N} , it is straightforward to solve Equation (4) for the best estimate of the true underlying map \mathbf{x} , which we denote as $\tilde{\mathbf{x}}$. Because we have noisy data, we can never find the exact underlying map. All *linear* solutions to this problem can be written in the form

$$\tilde{\mathbf{x}} = \mathbf{W}\mathbf{y}, \quad (5)$$

where \mathbf{W} is some $m \times n_t$ matrix. In general, the final map pixels in $\tilde{\mathbf{x}}$ will be correlated due to correlations from the signal, noise, and beam size. The correlations due to signal and beam size are kept in the *theory covariance matrix*, described in §5.1, whereas the noise correlations are recorded in the *map noise covariance matrix* Σ , which is defined as

$$\Sigma \equiv \mathbf{W}\mathbf{N}\mathbf{W}^t. \quad (6)$$

Note that the *total map covariance matrix*, \mathbf{C} , is the sum of signal plus noise: $\mathbf{C} \equiv \mathbf{S} + \Sigma$, where $\mathbf{S} \equiv \langle \mathbf{xx}^t \rangle$ is the theory covariance matrix. The total covariance matrix will be used in §5.

We desire to minimize the difference between $\tilde{\mathbf{x}}$ and \mathbf{x} ; that is, minimize $\langle |\epsilon|^2 \rangle$ where $\epsilon \equiv \tilde{\mathbf{x}} - \mathbf{x}$. A typical choice for \mathbf{W} is the COBE-style solution (Jansen & Gulkis 1992; Wright 1996), which gives $\mathbf{W} = [\mathbf{A}^t \mathbf{N}^{-1} \mathbf{A}]^{-1} \mathbf{A}^t \mathbf{N}^{-1}$. This is not the only \mathbf{W} you can choose, but it does have several nice properties. It minimizes $\langle |\epsilon|^2 \rangle$, subject to the constraint $\mathbf{W}\mathbf{A} = \mathbf{I}$. It is the maximum-likelihood estimate of \mathbf{x} , if the underlying probability distribution for \mathbf{n} is Gaussian. And finally, the reconstruction error ϵ is independent of the underlying map \mathbf{x} . For this solution, it can be shown that the mapmaking algorithm becomes

$$\Sigma = [\mathbf{A}^t \mathbf{N}^{-1} \mathbf{A}]^{-1} \quad (7a)$$

$$\tilde{\mathbf{x}} = \Sigma \mathbf{A}^t \mathbf{N}^{-1} \mathbf{y}. \quad (7b)$$

We will hereafter refer to the mapmaking solution with this particular choice of \mathbf{W} as *Minimum Variance Mapmaking*. The interested reader is referred to T97a for other noteworthy choices of \mathbf{W} .

The linear method (based on Equation (5)) is quite general, and can be applied to any type of problem where a linear combination of data is made in order to determine some physical parameter. Whenever the noise of said data isn't white, this is the best approach. For POLAR, we will exploit this technique no fewer than four different times throughout the analysis pipeline.

4.2. Mapmaking for POLAR

Let us now lay out the details of the mapmaking problem for the case of POLAR. We would like to obtain maps of Q and U for each of our three polarization channels (26–29, 29–32, and 32–36 GHz). If frequency-dependent foregrounds do not prove to be a problem, we can then average the maps of the three channels into final overall maps of Q and U , and proceed to do cosmology with those maps. Because of our scan strategy, a zenith drift scan at $\delta = 43^\circ$, our map will be a one-dimensional map in right ascension. Our beam was approximately 7° FWHM, so the number of independent pixels is $\frac{360}{7} \cos 43^\circ \sim 38$. As information can be lost if the pixels are too large, the general rule of thumb is to pixelize at $\sim 40\%$ of your beam FWHM or smaller, the so-called Shannon oversampling limit (de Oliveira-Costa et al. 1998). We chose to use 180, 2° RA-pixels, with the first pixel arbitrarily centered at RA = 0° .

The process begins with binning the data into our map coordinates. If data were taken in one long, continuous section (as from a balloon flight), it is possible to use Equation (7) to form the required pointing matrix and go straight to the final map. However, our data were taken in sections separated by periods of bad weather. Thus, it would have been possible to bin each night (or section) of data into map coordinates, but a significant difficulty arises with the noise properties of the data. For POLAR, our noise was only stationary over periods of tens of minutes; over longer periods, the fundamental power spectrum of the noise tended to change. Thus, we chose to form maps of the sky for each 7.5-minute (9000-sample) data file, in order to take advantage of the stationary noise property.

In principle, even nonstationary noise can be treated with the standard mapmaking formalism, but the algorithms are slow because \mathbf{N} has no special properties except that it is symmetric. The central rate determining step of the mapmaking algorithm of Equation (7) is in calculating \mathbf{N}^{-1} , the inverse of the 9000×9000 noise covariance matrix.

For stationary noise, however, the corresponding noise covariance matrix has the special property that it is both symmetric and *Toeplitz*; that is, each upper left–lower right diagonal is the same. Toeplitz matrices can be inverted in $\mathcal{O}(n_t^2)$ time, as opposed to $\mathcal{O}(n_t^3)$ for general $n_t \times n_t$ matrices (Golub & Van Loan 1996). However, the memory requirements are still $\mathcal{O}(n_t^2)$ because the inverse of a symmetric Toeplitz matrix is not in general Toeplitz. For POLAR, $n_t = 9000$, so simply holding the inverse matrix takes ~ 324 MB of memory for double-precision arithmetic. While not prohibitive, this memory requirement motivates further study of approximation techniques.

Tegmark (1997c) describes an approximation that reduces the computation time to $\mathcal{O}(n_t \log n_t)$, and also significantly reduces the memory requirements. He notes that a typical noise covariance matrix \mathbf{N} is nearly *circulant*, that is, each row equals the row above it with wrap-around boundary conditions. In this case, $\mathbf{N} = \mathbf{N}_c + \mathbf{N}_s$, where \mathbf{N}_c is the circulant component of \mathbf{N} and \mathbf{N}_s is the non-circulant component. As \mathbf{N}_c is the major contributor to \mathbf{N} , he lets $\mathbf{W} = [\mathbf{A}^t \mathbf{N}_c^{-1} \mathbf{A}]^{-1} \mathbf{A}^t \mathbf{N}_c^{-1}$. This solution is valid in that it still produces an unbiased, nearly-optimal approximation of the map, at the expense of slightly in-

creased noise.

A similar approach was used in the POLAR analysis. We discovered empirically that

$$\mathbf{b}_{pw} \equiv \mathbf{N}^{-1/2}\mathbf{b} \simeq \mathcal{F}^{-1} \left\{ \frac{\mathcal{F}\{\mathbf{b}\}}{\sqrt{S_N(f)}} \right\} \quad (8)$$

where \mathbf{b} is any vector of length n_t , \mathbf{N} is the $n_t \times n_t$ noise covariance matrix, $S_N(f)$ is the power spectral density that characterizes the noise, and “ \mathcal{F} ” denotes the Fourier Transform. This approach is advantageous in that it requires only a simple fit to the noise power spectrum for the time stream of interest; it is unnecessary to explicitly calculate the resulting covariance matrix \mathbf{N} . The resulting vector \mathbf{b}_{pw} is simply the prewhitened version of \mathbf{b} . Numerical tests showed that Equation (8) was accurate to within 1% for our data, fitted with a model of $1/f$ noise as well as our anti-aliasing filter:

$$S_N(f) = \sigma^2 \left(1 + \frac{f_{knee}}{f} \right) \left(1 + \left[\frac{f}{f_{crit}} \right]^\alpha \right)^{-1} \quad (9)$$

where f_{knee} is the knee frequency of the $1/f$ noise, $f_{crit} = 5$ Hz was the anti-aliasing filter cut-off frequency, and $\alpha \approx 7.5$ for the filters.

4.2.1. File-map Construction

It is then straightforward to apply our algorithms to the solution of the mapmaking problem, to form a small map for each data file and channel. For a given file, we have a timestream vector \mathbf{y} with $n_t = 9000$ samples. We will construct a map from this data covering the one or two pixels that were sampled by that file using the technique of Minimum Variance Mapmaking along with the fourier transform trick of Equation (8).

The Pointing Matrix

Our next task is to form the pointing matrix \mathbf{A} for the data file. \mathbf{A} is the transformation matrix that maps the sky map into our data stream; it depends only on the scan strategy and beam parameters. \mathbf{A} has a number of columns equal to the number of map pixels and a number of rows equal to the number of data samples.

The case of assembling \mathbf{A} for a one-horn total power experiment is particularly easy. For each row, you simply put a ‘1’ in the column of the pixel that this particular sample came from, and zeros everywhere else. Thus, \mathbf{A} is an exceedingly sparse matrix made up of 1’s and 0’s in the total power (intensity) case, such as most anisotropy experiments. A good example of this is given in Wright (1996), where the case of multiple horns is also treated.

Because of POLAR’s rotation and the fact that we are observing the Stokes parameters Q and U as well as the fictitious coefficients C and S (based on Equation (1)), our situation is somewhat more complicated. Let us write the map vector as $\mathbf{x} = \{\mathbf{c}, \mathbf{s}, \mathbf{q}, \mathbf{u}\}$. At some time t_i , the signal we observe is given by Equation (1). Now it is straightforward to form the pointing matrix \mathbf{A} , such that Equation (4) holds. Let us consider a toy model in which there are four sky pixels. Our map in this case is a 16-element vector, containing the parameters $\{c, s, q, u\}$ for each of the four pixels. For the observations \mathbf{y} within a data segment, a sample pointing matrix might look like the matrix in

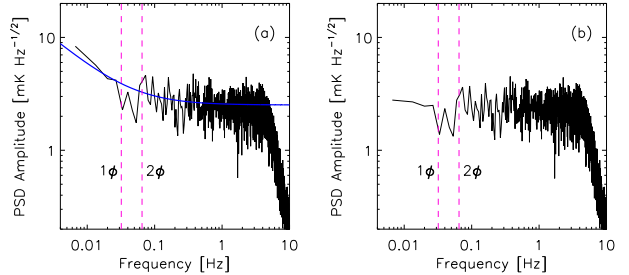


FIG. 7.— Effect of prewhitening on a sample noise power spectrum for channel J2i. Panel (a): PSD amplitude for a sample data file, with a knee frequency of ~ 0.07 Hz. The thick (blue) curve is the logarithmic-weighted fit to the PSD. The vertical dashed lines show the 1ϕ and 2ϕ rotational frequencies. Panel (b): Same as (a), but for the \mathbf{y}_{pw} version of the data. The effect was to whiten the power spectrum of the data; it is equivalent to dividing the PSD by the fitted curve.

Figure 6. In this example, for observations t_a through t_b , we were aimed at pixel 2, and likewise pixel 3 corresponds to $t_b + 1 - t_c$, and pixel 4 to $t_c + 1 - t_d$. Pixel 1 was included to show that we are not penalized for keeping extra pixels that do not contain any data; they simply get all 0’s in \mathbf{A} , and will have infinite error bars in the final map (however, it is easiest to throw those pixels out of the pointing matrix altogether). Then, by multiplying any row in \mathbf{A} (any column in \mathbf{A}^t) by the map vector \mathbf{x} , we recover Equation (1) in the absence of noise, which was our original goal.

Applying the Minimum Variance Mapmaking algorithm

Based on the chosen pixelization described above, only 1–2 pixels were observed per data file. We choose to solve for not only the Q and U maps, but also the fictitious C and S maps, in case there are important correlations between the 1ϕ and 2ϕ coefficients. Once \mathbf{A} is formed, we then fit for σ and f_{knee} using Equation (9), and apply Equation (8) to calculate the following quantities:

$$\mathbf{y}_{pw} \equiv \mathbf{N}^{-1/2}\mathbf{y} \quad (11a)$$

$$\mathbf{A}_{pw} \equiv \mathbf{N}^{-1/2}\mathbf{A} \quad (11b)$$

where the FFT trick is applied to each to each row of \mathbf{A} to form the corresponding row of \mathbf{A}_{pw} . Figure 7 shows a typical data vector \mathbf{y} and the corresponding prewhitened vector \mathbf{y}_{pw} . The model including the filter and $1/f$ noise is clearly a good fit to the noise (under the excellent assumption that the signal is negligible), correctly yielding a \mathbf{y}_{pw} that has a nearly white power spectrum.

Using these definitions, the Minimum Variance Mapmaking algorithm of Equation (7) becomes

$$\tilde{\mathbf{x}} = [\mathbf{A}_{pw}^t \mathbf{A}_{pw}]^{-1} \mathbf{A}_{pw}^t \mathbf{y}_{pw} \quad (12a)$$

$$\Sigma = [\mathbf{A}_{pw}^t \mathbf{A}_{pw}]^{-1}. \quad (12b)$$

By performing this algorithm on the data passing the cuts, we generated approximately 800 1–2 pixel maps in C , S , Q , and U , and all the corresponding intra-file correlations.

4.2.2. From File-maps to Submaps: How to Add Maps

Now we work our way up the “time-scale” ladder: for each section of data, we combine all the little 1–2 pixel

$$\mathbf{A}^t = \begin{pmatrix} 0 & 0 & \dots & 0 & 0 & \dots & 0 & 0 & \dots & 0 \\ \cos \phi_1 & \cos \phi_2 & \dots & \cos \phi_a & 0 & \dots & 0 & 0 & \dots & 0 \\ 0 & 0 & \dots & 0 & \cos \phi_{a+1} & \dots & \cos \phi_b & 0 & \dots & 0 \\ 0 & 0 & \dots & 0 & 0 & \dots & 0 & \cos \phi_{b+1} & \dots & \cos \phi_{N_f} \\ \hline 0 & 0 & \dots & 0 & 0 & \dots & 0 & 0 & \dots & 0 \\ \sin \phi_1 & \sin \phi_2 & \dots & \sin \phi_a & 0 & \dots & 0 & 0 & \dots & 0 \\ 0 & 0 & \dots & 0 & \sin \phi_{a+1} & \dots & \sin \phi_b & 0 & \dots & 0 \\ 0 & 0 & \dots & 0 & 0 & \dots & 0 & \sin \phi_{b+1} & \dots & \sin \phi_{N_f} \\ \hline 0 & 0 & \dots & 0 & 0 & \dots & 0 & 0 & \dots & 0 \\ \cos 2\phi_1 & \cos 2\phi_2 & \dots & \cos 2\phi_a & 0 & \dots & 0 & 0 & \dots & 0 \\ 0 & 0 & \dots & 0 & \cos 2\phi_{a+1} & \dots & \cos 2\phi_b & 0 & \dots & 0 \\ 0 & 0 & \dots & 0 & 0 & \dots & 0 & \cos 2\phi_{b+1} & \dots & \cos 2\phi_{N_f} \\ \hline 0 & 0 & \dots & 0 & 0 & \dots & 0 & 0 & \dots & 0 \\ \sin 2\phi_1 & \sin 2\phi_2 & \dots & \sin 2\phi_a & 0 & \dots & 0 & 0 & \dots & 0 \\ 0 & 0 & \dots & 0 & \sin 2\phi_{a+1} & \dots & \sin 2\phi_b & 0 & \dots & 0 \\ 0 & 0 & \dots & 0 & 0 & \dots & 0 & \sin 2\phi_{b+1} & \dots & \sin 2\phi_{N_f} \end{pmatrix} \quad (10)$$

FIG. 6.— A sample pointing matrix in the case of a 4-pixel sky, where the quantities $\{C, S, Q, U\}$ are measured for each pixel. \mathbf{A}^t is shown for simplicity.

file maps together into one map for each channel, and calculate its corresponding covariance matrix; these we call *submaps*. We find robustly that the “inter-coefficient correlations”, that is, correlations between any of the $Q, U, C,$ and $S,$ were completely negligible both within a pixel and between pixels. Because of this, we disregard the C and S data at this point; these coefficients do contain information on systematic effects, but making maps from them will be difficult to interpret and hence is not particularly informative.

We are thus faced with the standard “map combination” problem: given a collection of m independent maps $\{\mathbf{x}_1 \dots \mathbf{x}_m\}$ with corresponding noise covariance matrices $\{\mathbf{N}_1 \dots \mathbf{N}_m\}$, what is the best estimate of the full map? The problem is complicated by the fact that our maps are in general incomplete – each only covers a part of the total map.

Let us deal with the latter problem first. The solution to partial sky coverage is to “expand” each initial map to cover the final map by making up values for the unmeasured map pixels, but giving those values zero weight by assigning them infinite uncertainty in the noise covariance matrix. As an example, let us say one of our initial maps measures pixels 2 and 3 of a four-pixel map. We perform the following expansion of this initial map:

$$\mathbf{x}_i = \{x_2, x_3\} \rightarrow \{0, x_2, x_3, 0\} \quad (13)$$

and

$$\mathbf{N}_i = \begin{bmatrix} N_{11} & N_{12} \\ N_{21} & N_{22} \end{bmatrix} \rightarrow \begin{bmatrix} \infty & 0 & 0 & 0 \\ 0 & N_{11} & N_{12} & 0 \\ 0 & N_{21} & N_{22} & 0 \\ 0 & 0 & 0 & \infty \end{bmatrix} \quad (14a)$$

$$\text{and} \quad \mathbf{N}_i^{-1} \rightarrow \begin{bmatrix} 0 & 0 & 0 & 0 \\ 0 & N_{11}^{-1} & N_{12}^{-1} & 0 \\ 0 & N_{21}^{-1} & N_{22}^{-1} & 0 \\ 0 & 0 & 0 & 0 \end{bmatrix} \quad (14b)$$

Hence it is a trivial task to deal with the partial sky coverage problem. The inverse covariance matrix is important because that is what is actually used in the formalism (see Equation (15) below).

Now let us assume that the maps $\{\mathbf{x}_1 \dots \mathbf{x}_m\}$ and covariance matrices $\{\mathbf{N}_1 \dots \mathbf{N}_m\}$ have been expanded to all have equal coverage. How do we then find the minimum variance map containing all the information? The answer is, of course, Minimum Variance Mapmaking. We simply take our data vector to be $\mathbf{y} = \{\mathbf{x}_1 \dots \mathbf{x}_m\}$, and we form a block-diagonal “meta-covariance matrix” \mathbf{N} with all the little \mathbf{N}_i ’s on the diagonal. Since we’ve expanded each \mathbf{x}_i map to have the same pixel coverage as the final map we’re pointing to, each has a “pointing matrix” that is simply the n -element identity (assuming the maps all have n pixels). The full pointing matrix is then $\mathbf{A} = [\mathbf{I}, \dots, \mathbf{I}]$, so \mathbf{A} is a $(nm) \times n$ rectangular matrix. Applying the mapmaking formalism of Equation (7), it is straightforward to show that the final map \mathbf{x}_f and its associated covariance matrix \mathbf{N}_f are given by

$$\mathbf{N}_f = \left[\sum_{i=1}^m \mathbf{N}_i^{-1} \right]^{-1} \quad (15a)$$

$$\mathbf{x}_f = \mathbf{N}_f \left[\sum_{i=1}^m \mathbf{N}_i^{-1} \mathbf{x}_i \right] \quad (15b)$$

which is the standard result (*e.g.*, de Oliveira-Costa et al. (1998); Stompor et al. (2002)).

We applied this technique to all the data passing our cuts, in order to make a submap for each section, channel and $\{Q$ or $U\}$ combination, and for both the IPC and QPC channels: this generated approximately $6 \times 20 \times 2 = 240$ submaps on the sky.

4.3. The problem of the Q and U Offsets

At this point in the analysis, a serious issue revealed itself. The Q and U data in both the file maps and the submaps were not in general consistent with zero; there were offsets in Q and U that varied over the course of the season, and differed between the channels. This fact is illustrated in Figure 8, which shows the derived time stream of Q and U values for all the surviving data, for both the in-phase and quadrature-phase channels. In these

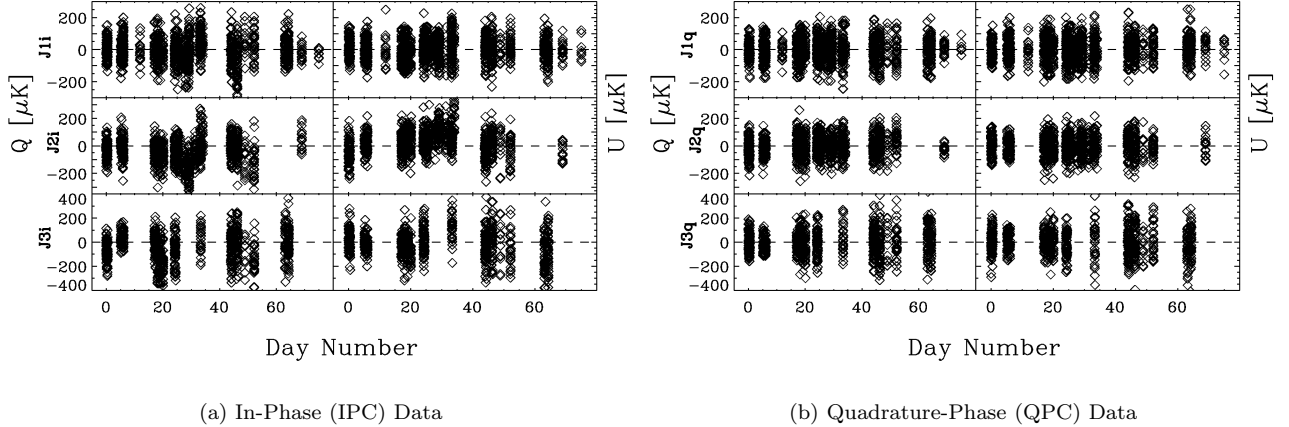


FIG. 8.— The mean values of Q and U for the POLAR data set versus time, after the cuts have been applied. Each data point represents one data file. Non-Gaussian behavior is immediately apparent at the 50-100 μK level in the (a) in-phase data, but is absent in the (b) quadrature-phase data.

plots, there is simply one value of Q and U for each data file. Notice first that the data lie in “chunks” along the time axis; each such chunk corresponds with what we have been calling “sections”. The distribution of Q ’s and U ’s for each section is consistent with a Gaussian distribution, but those distributions are in general not centered around zero. Figure 8(b) shows this same information for the quadrature-phase channels; this data was consistent with being offset-free. Therefore, the offset was not electronic in nature, but the values of it were too high to be consistent with any kind of believable signal, and also were not consistent with a celestial signal when plotted in sky coordinates.

The underlying cause of the offset was never discovered, but there are several reasonable possibilities. K02 hypothesizes that the quadrupolar shape of the outer ground-screen may be to blame (Keating et al. 2002). O’Dell (2001) examines the characteristics of the offsets in great detail, as well as providing several theories for the possible cause; the interested reader is referred to these sources for more detail.

4.4. Offset Removal Techniques

Whatever the ultimate cause of the offsets, it is clear that something must be done about them in order to proceed with the data analysis. If we had some model of the effects that could make successful predictions about its level, we could use it to safely subtract out the offsets without strongly affecting our signal recovery. However, without such a model we must proceed along a different path, which assumes no knowledge of the offset cause.

Most experiments have offsets that they must treat, and as such significant analytical machinery has been developed to account for this contingency. The topic was apparently first addressed in a mathematically consistent way by Rybicki and Press (Rybicki & Press 1992; Press et al. 1992). de Oliveira-Costa et al. (1998) introduced the method of *virtual pixels* (sometimes called “extra pixels”) to estimate and remove offsets, while Tegmark (1997b) derived tricks for the removal of unwanted modes in CMB

maps, although the techniques are quite general. BJK98 introduced the method of *marginalization* (or “constraint matrices”), where unwanted modes of a time stream or map have infinite noise added to them, thus removing them. Recently, the DASI group used the BJK technique to deal with their offset problems (Halverson et al. 2002), while the MAXIMA group explored both virtual pixels and marginalization, and provide a review of these techniques in S02.

Although the mechanics of the two primary mode-removal techniques, the Tegmark-QMAP technique of virtual pixels and the BJK technique of marginalization, are quite different, they produce identical results. Typically one or the other is more convenient, depending on the situation. We will briefly explore each of these methods below; our discussion draws heavily upon S01, to which the reader is referred if more details are required.

4.4.1. Direct Offset Removal (Virtual Pixels)

Let us first define the problem. Consider a data vector \mathbf{y} and corresponding noise covariance matrix \mathbf{M} . \mathbf{y} may correspond to a map, submap, or to time-ordered data; it does not matter. We begin by treating the case of a simple offset, but generalize this to more complicated modes (*e.g.* a linear term). First, what is the offset in \mathbf{y} , *i.e.*, what is its weighted mean? The easiest way to calculate this is using Minimum Variance Mapmaking again, but taking the resultant “map” to be a single number. Using this approach it can be shown that for a data vector \mathbf{y} with noise covariance \mathbf{N} , the weighted mean is given by

$$\langle \mathbf{y} \rangle = [\mathbf{e}_0^t \mathbf{N}^{-1} \mathbf{e}_0]^{-1} \mathbf{e}_0^t \mathbf{N}^{-1} \mathbf{y} \quad (16)$$

where \mathbf{e}_0 is a column vector of all 1’s. Notice that \mathbf{e}_0 is our pointing matrix in this case – it “points” to only one pixel, the mean. Similarly, the data with the mean removed is given by

$$\mathbf{y} - \langle \mathbf{y} \rangle = \mathbf{\Pi} \mathbf{y} \quad (17a)$$

$$\mathbf{\Pi} \equiv \mathbf{I} - \mathbf{e}_0 [\mathbf{e}_0^t \mathbf{N}^{-1} \mathbf{e}_0]^{-1} \mathbf{e}_0^t \mathbf{N}^{-1}. \quad (17b)$$

We have intentionally expressed this relation as some matrix $\mathbf{\Pi}$ operating on the data vector; it is inordinately

handy to use an *operator* that extracts the weighted mean of something, and have that operator be independent of the data itself (it only depends on the noise properties of the data). Note that $\mathbf{\Pi}$ is not in general symmetric. The covariance matrix of the new data set $\mathbf{y} - \langle \mathbf{y} \rangle$ can then be calculated:

$$\mathbf{C} \equiv (\mathbf{y} - \langle \mathbf{y} \rangle)(\mathbf{y} - \langle \mathbf{y} \rangle)^t = \mathbf{\Pi} \mathbf{N} \mathbf{\Pi}^t = \mathbf{\Pi} \mathbf{N} = \mathbf{N} \mathbf{\Pi}^t \quad (18)$$

where the final two equalities are easily shown given the definition of $\mathbf{\Pi}$ given in Equation (17).⁵

It turns out that \mathbf{C} is singular; this is a consequence of the fact that we have lost sensitivity to the mean of \mathbf{y} , which directly leads to a zero eigenvalue in \mathbf{C} . However, for the purposes of a likelihood analysis, all that is needed is the “pseudo-inverse” of \mathbf{C} , which we denote as \mathcal{C}^{-1} :

$$\mathcal{C}^{-1} \equiv \mathbf{N}^{-1} \mathbf{\Pi} = \mathbf{\Pi}^t \mathbf{N}^{-1} . \quad (19)$$

This cannot be the true inverse of \mathbf{C} , but it is true that $\mathbf{\Pi} [\mathbf{C} \mathcal{C}^{-1} - \mathbf{I}] = \mathbf{0}$, which means that \mathcal{C}^{-1} is the inverse of \mathbf{C} once we project out the unwanted mean (Tegmark 1997b).

This method can be directly extended to allow for elimination of any unwanted modes in a data stream or map, such as a linear or quadratic term. In that case, we construct a $m \times n$ matrix, \mathbf{Z} , where n is the number of data/map elements, and m is the number of modes. Each column of \mathbf{Z} contains the template for that mode⁶. We then simply replace \mathbf{e}_0 with \mathbf{Z} in each of the above equations, and everything still works.

The mode-removed data vector $\mathbf{\Pi} \mathbf{y}$ and associated noise matrix \mathbf{C} have another property worth discussing. When calculating the likelihood function for some model, what we really care about is the χ^2 of the data, defined in general as $\mathbf{y}^t \mathbf{N}^{-1} \mathbf{y}$ for a data vector \mathbf{y} and covariance matrix \mathbf{N} . After mode removal, the χ^2 is given by:

$$\begin{aligned} \chi^2 &= (\mathbf{\Pi} \mathbf{y})^t \mathbf{N}^{-1} \mathbf{\Pi} (\mathbf{\Pi} \mathbf{y}) \\ &= \mathbf{y}^t (\mathbf{\Pi}^t \mathbf{N}^{-1} \mathbf{\Pi}) \mathbf{y} \\ &= \mathbf{y}^t \mathcal{C}^{-1} \mathbf{y} . \end{aligned} \quad (20)$$

The point here is that we only need to change the data covariance matrix to get the same χ^2 ; we don’t need to modify the data vector \mathbf{y} at all. We can determine the unwanted modes and subtract them out, but it simply does not matter; any final model predictions will be the same.

4.4.2. Marginalization and Constraint Matrices

Our last discovery lends understanding to the BJK marginalization technique for removing unwanted modes from a data set. The standard formulation of this technique is as follows. Given data \mathbf{y} and covariance matrix \mathbf{N} , one simply adds “constraint matrices” to the covariance matrix to *remove sensitivity to unwanted modes* (Bond et al. 1998):

$$\mathbf{N}_t = \mathbf{N} + \sigma_c^2 \mathbf{Z} \mathbf{Z}^t \quad (21)$$

where \mathbf{Z} is the again the template of the unwanted mode(s), and σ_c^2 represents the variance of the unknown amplitude of the modes. Recall that in the case of removing a single

⁵ It can also be shown that $\mathbf{\Pi}^2 = \mathbf{\Pi}$.

⁶ \mathbf{Z} is simply the pointing matrix that “points” to the modes we wish to subtract; each mode is represented by a single “pixel” in this bizarre map space.

offset, $\mathbf{Z} = \mathbf{e}_0$. One then takes σ_c^2 to be much larger than the instrument noise, so these unwanted modes get zero weight, but not large enough to cause matrix inversion problems.

Formally, one can also take the limit as $\sigma_c^2 \rightarrow \infty$. In that case, \mathbf{N}_t has an infinite eigenvalue, but its inverse still exists and is given by

$$\mathbf{N}_t^{-1} = \mathbf{N}^{-1} - (\mathbf{N}^{-1} \mathbf{Z}) [\mathbf{Z}^t \mathbf{N}^{-1} \mathbf{Z}]^{-1} (\mathbf{N}^{-1} \mathbf{Z})^t . \quad (22)$$

The astute reader will notice that this is *identical* to Equation (19) (replacing \mathbf{e}_0 ’s with \mathbf{Z} ’s), which gave the pseudo-inverse of the corrected covariance matrix in the technique that directly subtracted off the mean (or other unwanted modes). Thus, both the method of virtual pixels and the BJK marginalization technique yield the same inverse data covariance matrix in the limit that $\sigma_c^2 \rightarrow \infty$. They do, however, result in different data covariance matrices; that is, $\mathbf{C} \neq \mathbf{N}_t$ based on Equations 18 and 21. Although the corrected covariance matrix is a necessary ingredient in the likelihood analysis (see Equation (30)), it will not matter in the end which technique is used, because these two matrices only differ with respect to the modes that have been subtracted out⁷.

4.5. From Submaps to Final Maps

The application of the algorithms described in the previous section for offset removal is quite straightforward, at least to construct the mean-removed submaps. For POLAR, an offset was subtracted in both Q and U , because these are independent variables with no clear systematic relationship between their offsets. These offsets are removed for each of the three IPC as well as QPC channels, because as described previously there was no clear relationship between the offsets of the different channels that could be exploited.

4.5.1. How to Combine Maps with Singular Inverse Covariance Matrices

We have done a substantial amount of data processing in our march from time-ordered data to final maps. We currently have a set of submaps and their corresponding covariance matrices for each channel, for both Stokes Q and U . For each channel, we shall now combine the submaps together into a single map and covariance matrix. §4.2.2 describes the machinery to perform this step: we simply apply Equation (15) to our set of submaps (for Q and U and for each channel, of course), with one complicating factor – the covariance matrices for each submap have singular inverses, due to the offset removal step. That is alright, because we know the (pseudo-)inverse matrices explicitly from Equation (22).

However, we still have to perform a final inversion to find the final noise covariance matrix, which from Equation (15) is $[\sum_{i=1}^m \mathbf{N}_i^{-1}]^{-1}$; this sum in is in general singular. As we have removed the unwanted modes from our maps, the final map also has the same unwanted modes removed, and hence has infinite eigenvalues in its covariance matrix – *i.e.*, its covariance matrix does not formally exist. But these modes contain no information, so we are free to set their eigenvalues to whatever we like, as long as we take

⁷ To be more precise, the corrected matrix \mathbf{C} has eigenvalues equal to zero for the removed modes, while \mathbf{N}_t has eigenvalues of order σ_c^2 .

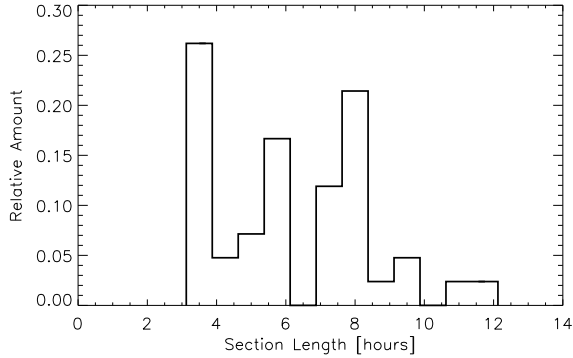


FIG. 9.— Distribution of Surviving Section Lengths. The distributions for each of the three channels have been averaged, as they are slightly different due to the different cuts each channel undergoes. Clearly there are several surviving sections with a mere 3-5 hours of data, resulting in a significant information loss due to offset removal.

care to remember what we have done in future processing. If we denote the final covariance matrix as Σ , such that $\Sigma^{-1} = [\sum_{i=1}^m \mathbf{N}_i^{-1}]$, then the final covariance matrix is taken to be

$$\Sigma = (\Sigma^{-1} + \epsilon \mathbf{Z}\mathbf{Z}^t)^{-1} - \epsilon^{-1} \mathbf{Z}\mathbf{Z}^t \quad (23)$$

where ϵ is any small positive number. In practice, it is best to choose ϵ to be of the same order as the nonzero eigenvalues of Σ^{-1} . The trick performed in Equation (23) replaces the infinite eigenvalue(s) in Σ with zero eigenvalue(s); all the information in the other modes of the matrix remains unchanged. This will have consequences for any type of further analysis. In performing any likelihood analysis one forms the full covariance matrix (\mathbf{C}) by adding together the covariance matrices from theory (\mathbf{S}) and data (Σ):

$$\mathbf{C} = \mathbf{S} + \Sigma \quad , \quad (24)$$

but we have explicitly set the infinite eigenvalue of Σ to zero, so it is quite possible that \mathbf{C} will also have a zero eigenvalue. In any likelihood analysis we will have to invert \mathbf{C} , which we can perform as follows:

$$\mathbf{C}^{-1} = \lim_{\sigma^2 \rightarrow \infty} [\mathbf{S} + \Sigma + \sigma^2 \mathbf{Z}\mathbf{Z}^t]^{-1} \quad . \quad (25)$$

All we are doing in this equation is adding back in the large uncertainty to the modes which are supposed to have infinite eigenvalues, which we had previously set to zero. In practice, we take σ^2 to be much larger than any of the other eigenvalues of Σ to ensure the unwanted modes get zero weight. Recall that in the simple case of offset removal, $\mathbf{Z}\mathbf{Z}^t$ is just the matrix of all 1's, so all we are doing is playing with the overall offset of the covariance matrix.

4.5.2. A Brief Comment on Information Loss

For the 7° beamsize of POLAR, we stared at one true 7° pixel roughly every 47 minutes (this is $\sim 10^\circ$ in right ascension). The surviving data from each section varied in duration; we required it to be at least 3 hours long, and the longest was about 8 hours long; the distribution of section lengths (averaged between the three channels) is shown in Figure 9.

For a short section containing, for instance, only four independent pixels, we naively seem to remove $\sim 25\%$ of its information when we remove its offset. However, the central lobe of the theory covariance matrix is not 10° FWHM in right ascension (as is the beam), it is roughly 25° (see Figure 12). Instead of removing 25% of the information, we have removed closer to 60% for the case of constraining the flat band-power model of §5.1. It is important to bear this penalty in mind. If we instead had further chopped up our data into smaller sections, removed more terms, etc., the information loss would have been correspondingly worse. This emphasizes to the experimenter that having long, clean sections of data is key to obtaining the best final noise possible, especially if any kind of mode removal may take place in the analysis.

4.5.3. Qualitative Analysis of the Final Maps

The final maps for POLAR for each of our three frequencies were constructed according to the recipe given above, and were initially presented in K01. Qualitatively, there is not strong evidence of a common signal among the three sub-bands, in either Q or U . The χ^2 values from each map, shown in Table 3, are also not consistent with a statistically significant signal. Let us additionally consider the corresponding maps made from the QPC channels. We do not expect these to contain signals, but rather they serve as a useful litmus test when viewing the IPC maps: if the IPC maps differ strongly from the QPC maps, that is evidence of either signal or some type of contamination. However, that is not the case; none of the maps contain strong outliers, and all exhibit χ^2 values consistent with zero signal.

4.5.4. Combining the Channel Maps

Based on the fact that there is no apparent correlation between the maps of each channel, we will simplify the likelihood analysis by combining the three channel maps into one combined map (and covariance matrix). Since the CMB signal is independent of frequency in the Rayleigh-Jeans regime, we are free to do this. We would like to employ the standard map co-addition algorithm introduced in §4.2.2 to perform this task. However, that algorithm assumes that the measurements made of each individual map are *independent*; if there is a systematic effect that

TABLE 3
 χ^2 VALUES FOR THE IPC AND
QPC CHANNEL MAPS.

	Q	U
J1i	41.1/41	39.3/41
J2i	44.0/41	47.6/41
J3i	52.3/41	55.1/41
J1q	44.2/41	45.5/41
J2q	40.8/41	42.9/41
J3q	47.1/41	30.9/41

NOTE: In the (reduced) χ^2 values displayed above, the number of degrees of freedom was 41. For a map \mathbf{x} with covariance matrix \mathbf{N} , we use the standard definition $\chi^2 = \mathbf{x}^t \mathbf{N}^{-1} \mathbf{x}$.

introduces correlations between measurements from different channels, then we have less information than we think we do, and this fact must be taken into account in constructing the summed map.

We first evaluated the correlation coefficients among channels J1i, J2i, and J3i in the time-ordered data. As expected, the correlations in the time stream were on the order of 1%, and were due to the very slight overlap of the three channels in frequency space (see K02 for details). However, it is not the time stream correlations that we so much care about, it is the correlations between Q or U for the channels. For instance, if there were a 10% correlation between J1i- Q and J2i- Q , it could be hidden in the smaller time stream correlations. We must therefore evaluate these correlations directly.

In order to measure these correlations, we used the Q and U data set and determined the Pearson’s correlation coefficient in the same way as for the time-ordered data, but because there is so much less data, we evaluated only one correlation coefficient for each surviving section. We then calculated means and errors by averaging from the distribution of these values. Table 4 shows these correlation coefficients with their errors. The numbers in this table are very suggestive. For instance, $\langle Q Q \rangle$ for all IPC channels is about the same as $\langle U U \rangle$, suggesting a common source. All QPC correlation coefficients are consistent with zero, as are all correlations of the $\langle Q U \rangle$ variety⁸. As Q and U show no correlation between them (either within a channel or between channels), we can continue treating Q and U as completely independent measurements. This is not too surprising, considering they are essentially the $\sin 2\phi$ and $\cos 2\phi$ projections from each rotation, which are orthogonal functions. However, the correlations between IPC channels (for the same Stokes parameter) are $\sim 10\%$, so we cannot ignore them in constructing a final map.

Let us now combine the maps of Q (or U) from the three non-independent channels, armed with the knowledge of their mutual correlations. The algorithms in §4.2.2 did not deal with adding non-independent maps together, but it is relatively easy to expand the methods to do so. We treat Q and U separately, as they are completely uncorrelated. Let us consider our situation for Q (U will follow an identical format).

We have three channel maps, call them \mathbf{x}_1 , \mathbf{x}_2 , and \mathbf{x}_3 ,

⁸ Except perhaps $\langle Q_1 U_3 \rangle$, but because all the other coefficients of this type are consistent with zero, we assume it is an outlier.

TABLE 4

INTER-CHANNEL CROSS-CORRELATION COEFFICIENTS
CALCULATED FROM THE SURVIVING Q AND U DATA.^a

	$\langle QQ \rangle$	$\langle UU \rangle$	$\langle QU \rangle$	$\langle UQ \rangle$
$\langle \mathbf{J1 J2} \rangle_{\text{IPC}}$	0.144 ± 0.034	0.134	-0.024	0.021
$\langle \mathbf{J1 J2} \rangle_{\text{QPC}}$	0.005 ± 0.034	0.062	-0.011	-0.002
$\langle \mathbf{J1 J3} \rangle_{\text{IPC}}$	0.074 ± 0.041	0.063	-0.069	-0.003
$\langle \mathbf{J1 J3} \rangle_{\text{QPC}}$	0.023 ± 0.041	0.048	-0.009	-0.042
$\langle \mathbf{J2 J3} \rangle_{\text{IPC}}$	0.104 ± 0.041	0.093	-0.024	-0.029
$\langle \mathbf{J2 J3} \rangle_{\text{QPC}}$	0.066 ± 0.041	0.001	-0.054	-0.047

^a The errors are the same within each row, and we assume that the underlying distribution of correlation coefficients is Gaussian.

with their corresponding covariance matrices Σ_1 , Σ_2 , and Σ_3 . Let the correlation coefficient between \mathbf{x}_i and \mathbf{x}_j be ρ_{ij} . We appeal to Minimum Variance Mapmaking to form the best possible map. First, we form the “meta-map”, which is the three maps concatenated together, and a corresponding “meta-covariance matrix”:

$$\mathbf{x}_{meta} = \{\mathbf{x}_1, \mathbf{x}_2, \mathbf{x}_3\} \quad (26a)$$

$$\Sigma_{meta} = \begin{bmatrix} \Sigma_1 & \rho_{12}\Sigma_{12} & \rho_{13}\Sigma_{13} \\ \rho_{12}\Sigma_{12} & \Sigma_2 & \rho_{23}\Sigma_{23} \\ \rho_{13}\Sigma_{13} & \rho_{23}\Sigma_{23} & \Sigma_3 \end{bmatrix} \quad (26b)$$

where $\Sigma_{ij} \equiv \sqrt{\Sigma_i}\sqrt{\Sigma_j}$. We can take the square roots of the Σ -matrices since they are all positive definite, as long as we add a large offset to each matrix (corresponding to the uncertainty in the offset, which is formally infinite)⁹. The final full covariance matrix, Σ_f , will then also have a large offset, but because of the arguments already discussed, this will not affect the final CMB likelihood analysis. We simply must remember that the very large eigenvalue of the final map covariance matrix represents our infinite uncertainty in the overall map offset.

Now that we have re-expressed our individual maps in concatenated (or “meta”) format, we apply the Minimum Variance Mapmaking formalism. The pointing matrix is given by

$$\mathbf{A}_{meta} = \begin{bmatrix} \mathbf{I}_n \\ \mathbf{I}_n \\ \mathbf{I}_n \end{bmatrix}. \quad (27)$$

This points our three individual maps to the same final map; each \mathbf{I} is the $n \times n$ identity matrix, where n is the number of pixels in our maps. Explicitly, the final joint map and covariance matrix are given by:

$$\mathbf{x}_f = \Sigma_f \mathbf{A}_{meta}^t \Sigma_{meta}^{-1} \mathbf{x}_{meta} \quad (28a)$$

$$\Sigma_f = [\mathbf{A}_{meta}^t \Sigma_{meta}^{-1} \mathbf{A}_{meta}]^{-1}. \quad (28b)$$

Because of the large offset each covariance matrix possesses, the final map \mathbf{x}_f may have some random offset to it, but it is meaningless, and can be safely subtracted out. Notice that in the case of vanishing inter-map correlations, we correctly reproduce the results of §4.2.2.

The final joint-maps for the IPC and QPC are shown in Figure 10. There is no obvious evidence of an underlying sky signal. In order to determine robustly if they show evidence of a sky signal, we employ the standard maximum likelihood and quadratic estimators techniques in order to constrain specific models of CMB polarization, described fully in §5.

4.6. Testing the Mapmaking Pipeline

In any experiment, it is often useful to simulate as much of it as possible in order to uncover errors in the analysis pipeline, or to find ways to optimize aspects of the system. For POLAR, we simulated the data stream in order to test the map reconstruction pipeline, to verify that the recipe outlined above works as advertised. There were three primary steps involved in the simulation process: build the underlying map, let POLAR “observe” this fake sky and

⁹ For a symmetric, positive-definite, $n \times n$ matrix \mathbf{M} , its square root is given by $\mathbf{P}^t \mathbf{D}^{1/2} \mathbf{P}$, where \mathbf{P} is an $n \times n$ matrix such that the i^{th} row of \mathbf{P} contains the i^{th} eigenvector of \mathbf{M} , and $\mathbf{D}^{1/2}$ is a diagonal matrix with the square-roots of the eigenvalues of \mathbf{M} along its diagonal. The eigenvectors must be normalized, such that $\mathbf{P}\mathbf{P}^t = \mathbf{I}$.

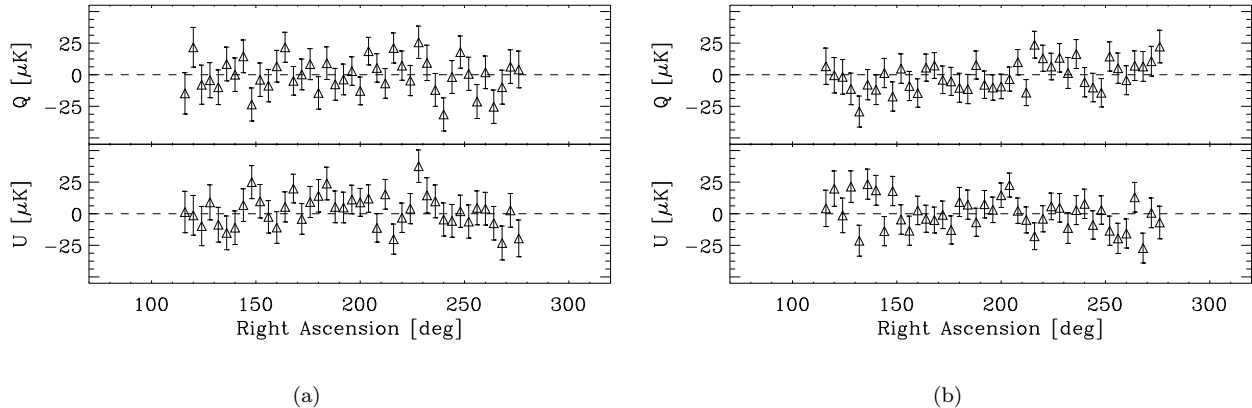


FIG. 10.— Final joint-channel sky maps. The joint IPC maps for Q and U are displayed in (a), while (b) shows the QPC maps.

generate data based on these observations, and construct maps from the resulting data set. We built the underlying sky maps out of simple sine and cosine modes, for both total intensity (I) and Stokes Q and U . We assumed a basic flat band-power model with $\sim 10 \mu K$ per band, and convolved these signals with our 7° (FWHM) Gaussian beam. This signal level is of course highly unrealistic for true CMB polarization; we used it merely so we could reconstruct the actual map with good signal-to-noise (instead of merely providing an upper limit).

To shorten processing time, we made the simulated instrument about a factor of two more sensitive than the real POLAR, with a full-band sensitivity of $340 \mu K \sqrt{\text{sec}}$. We included all IPC and QPC channels in the analysis, but no total power channels. We assumed the noise was almost white, with a small amount of $1/f$ noise in each channel in agreement with the true data set. We convolved each data stream with our 5 Hz anti-aliasing filter to ensure a resulting power spectrum that was similar to the actual data. We also added random offsets in I , Q , and U for each section and channel, of levels consistent with those experienced by POLAR. We generated five sections of data, with a total of 31 hours of observation time, giving each section a different set of offsets. The simulation parameters for each channel are shown in Table 5.

We next ran the simulated POLAR signals through the full analysis pipeline (including the offset removal) for all channels, in both Q and U . The derived joint-channel maps are shown in Figure 11, along with the underlying sky maps for comparison. The performance of the analysis software was good; the derived maps match the initial maps well, up to an overall offset; the offset is meaningless because we have lost sensitivity to it, and this information is encoded in the final covariance matrix. The reduced χ^2 values are also shown, and are close to unity in each case. The QPC maps were consistent with noise. These results lend strong support to the validity of our map reconstruction algorithms.

5. CONSTRAINING CMB POLARIZATION MODELS

5.1. Limits on E and B in a Flat Band-Power Model

Because no signal is evident in the maps shown in Figures 10(a) and (b), we begin with a very simple question: What is the rms polarization in the maps? A robust yet simple way to answer this question is using the framework of a maximum likelihood analysis; for the beginner, an excellent discussion of how to carry out such an analysis is provided in Bunn (1993).

As POLAR measured both Stokes Q and U simultaneously, we are able to set limits on both E - and B -type polarization independently. As described previously in K01, we shall constrain a flat CMB power spectrum, characterized by two polarization temperatures T_E and T_B such that

$$\ell(\ell + 1)C_\ell^X / 2\pi = T_X^2 \quad (29)$$

where $X \in \{E, B\}$. We then solve for the likelihood function $\mathcal{L}(\vec{a})$, given by

$$\mathcal{L}(\vec{a}) \propto \frac{e^{-\frac{1}{2}\mathbf{x}^t \mathbf{C}^{-1}(\vec{a})\mathbf{x}}}{|\mathbf{C}(\vec{a})|^{1/2}}, \quad (30)$$

where \vec{a} is our parametrization vector $\vec{a} \equiv \{T_E, T_B\}$, $\mathbf{x} = \{\mathbf{q}, \mathbf{u}\}$ is the concatenation of the joint channel maps of Q and U given in the previous section, and $\mathbf{C}(\vec{a})$ is the full

TABLE 5
SIMULATION PARAMETERS FOR EACH CORRELATOR CHANNEL.

Channel	NET (mK s ^{1/2})	1/f Knee (Hz)	I_0 ^a (mK)	Q_0 ^a (μK)	U_0 ^a (μK)
J1i	0.50	0.01	3r	30r	20r
J2i	0.55	0.005	10r	60r	40r
J3i	0.80	0.02	50r	90r	60r
J1q	0.50	0.01	0.03r	0	0
J2q	0.55	0.005	0.1r	0	0
J3q	0.80	0.02	0.5r	0	0

^a The “r” indicates a random number between -1 and 1 , drawn from a flat distribution. Thus, for example, the offsets Q_0 for channel J1i were between -30 – $30 \mu K$, and were different for each section. The QPC were found to have offsets ~ 100 times less than the IPC for the actual POLAR instrument, reflected in their offsets above.

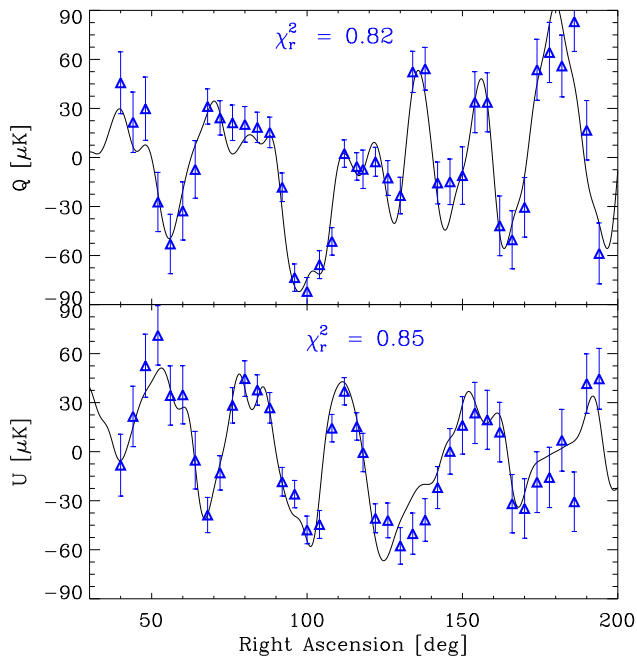


FIG. 11.— Derived joint-channel maps for simulated data, for the IPC channels, compared to the underlying sky map. The thin (black) curve is the underlying sky map convolved with a 7° beam. The (blue) data points represent the derived joint-channel map, after the 31 hours of simulated data were run through the POLAR mapmaking pipeline. The fairly high signal-to-noise ratio is due to the excellent noise figures we assumed for the simulated experiment, coupled with the high underlying signal strength.

covariance matrix given by the sum of the data (or noise) and theory covariance matrices:

$$\mathbf{C}(\vec{a}) = \mathbf{S}(\vec{a}) + \mathbf{\Sigma}. \quad (31)$$

The data covariance matrix $\mathbf{\Sigma}$ is formed from the covariance matrices for the joint-channel maps of Q and U such that

$$\mathbf{\Sigma} = \begin{bmatrix} \mathbf{\Sigma}_Q & 0 \\ 0 & \mathbf{\Sigma}_U \end{bmatrix}. \quad (32)$$

5.1.1. Evaluating the Theory Covariance Matrix

Unfortunately, the construction of the theory covariance matrix \mathbf{S} is not quite as simple; its derivation is introduced in Zaldarriaga (1998), and described in great detail in Tegmark & de Oliveira-Costa (2001). If N is the number of pixels in each of the Q and U maps, then \mathbf{S} is a $2N \times 2N$ matrix, which we will consider as an $N \times N$ matrix whose elements are themselves 2×2 matrices. The 2×2 elemental matrix \mathbf{S}_{ij} describes the covariance between two pixels i and j , and is given by

$$\mathbf{S}_{ij} = \langle \mathbf{x}_i \mathbf{x}_j \rangle = \mathbf{R}(\alpha_{ij}) \mathbf{M}(\hat{\mathbf{r}}_i \cdot \hat{\mathbf{r}}_j) \mathbf{R}(\alpha_{ij})^t \quad (33)$$

where $\hat{\mathbf{r}}_i$ and $\hat{\mathbf{r}}_j$ are the unit vectors pointing to pixels i and j , respectively. $\mathbf{R}(\alpha_{ij})$ is a standard rotation matrix which rotates the (Q, U) components in \mathbf{M} into the global coordinate system where the reference frame for Q and U is given by the local meridian; it is given by

$$\mathbf{R}(\alpha) = \begin{pmatrix} \cos 2\alpha & \sin 2\alpha \\ -\sin 2\alpha & \cos 2\alpha \end{pmatrix}. \quad (34)$$

The covariance matrix \mathbf{M} depends only on the angular separation between the pixels i and j . \mathbf{M} is most naturally

expressed in a coordinate system such that the great circle connecting pixels i and j serves as the reference axis for the Stokes parameters (Kamionkowski et al. 1997). Expressed in this coordinate frame, \mathbf{M} becomes (Zaldarriaga 1998)

$$\mathbf{M}(\hat{\mathbf{r}}_i \cdot \hat{\mathbf{r}}_j) \equiv \begin{pmatrix} \langle Q_i Q_j \rangle & 0 \\ 0 & \langle U_i U_j \rangle \end{pmatrix}, \quad (35)$$

$$\langle Q_i Q_j \rangle \equiv \sum_{\ell} \frac{2\ell + 1}{4\pi} B_{\ell}^2 [F_{\ell}^{12}(z) C_{\ell}^E - F_{\ell}^{22}(z) C_{\ell}^B] \quad (36a)$$

$$\langle U_i U_j \rangle \equiv \sum_{\ell} \frac{2\ell + 1}{4\pi} B_{\ell}^2 [F_{\ell}^{12}(z) C_{\ell}^B - F_{\ell}^{22}(z) C_{\ell}^E] \quad (36b)$$

where $z = \hat{\mathbf{r}}_i \cdot \hat{\mathbf{r}}_j$ is the cosine of the angle between the two pixels under consideration, $B_{\ell} = \exp[-\ell(\ell + 1)\sigma_B^2/2]$, σ_B is the beam dispersion = $0.425 \times \text{FWHM}$, and $F_{\ell}^{12}, F_{\ell}^{22}$ are functions of Legendre polynomials as defined in Zaldarriaga (1998) and Tegmark & de Oliveira-Costa (2001). The full matrix \mathbf{S} is then constructed by looping over all necessary pixel pairs. In principle, \mathbf{S} needs to be calculated for all (T_E, T_B) combinations in order to fully assess the likelihood function. However, there is a great simplification lurking here. Utilizing Equation (29), Equation (33) can be recast as

$$\mathbf{S}_{ij} = T_E^2 \mathbf{S}_{ij}^E + T_B^2 \mathbf{S}_{ij}^B, \quad (37)$$

$$\mathbf{S}_{ij}^X \equiv \mathbf{R}(\alpha_{ij}) \sum_{\ell} \frac{2\ell + 1}{2\pi\ell(\ell + 1)} B_{\ell}^2 \mathbf{F}_{\ell}^X(z) \mathbf{R}(\alpha_{ij})^t \cdot (1 \mu K^2) \quad (38)$$

where

$$\mathbf{F}_{\ell}^E(z) \equiv \begin{bmatrix} F_{\ell}^{12}(z) & 0 \\ 0 & -F_{\ell}^{22}(z) \end{bmatrix} \quad \text{and} \quad \mathbf{F}_{\ell}^B(z) \equiv \begin{bmatrix} -F_{\ell}^{22}(z) & 0 \\ 0 & F_{\ell}^{12}(z) \end{bmatrix}. \quad (39a)$$

The theory covariance matrix \mathbf{S} in the flat band-power model is then given by

$$\mathbf{S}(T_E, T_B) = T_E^2 \mathbf{S}^E + T_B^2 \mathbf{S}^B \quad (40)$$

where \mathbf{S}^E is the *fundamental* theory covariance matrix for purely E -modes, comprised of all the 2×2 \mathbf{S}_{ij}^E matrices, and similarly for \mathbf{S}^B . Now we must merely calculate \mathbf{S}^E and \mathbf{S}^B once each, and we can then evaluate the full theory covariance matrix for any (T_E, T_B) pair we like using Equation (40).

The signal covariance matrices were calculated for our 2° pixelization spanning all 360° of right ascension, using as an approximation to our beam a single 7° FWHM Gaussian, in order to calculate our beam function B_{ℓ} for use in Equations (36); this beam function was shown in both K98 and O'Dell (2001), and is essentially our window function for the flat band-power model. A representative row from both fundamental signal covariance matrices, \mathbf{S}^E and \mathbf{S}^B , is shown in Figure 12. This shows the covariance between the pixel at right ascension 40° and all the other pixels. Notice how wide the main peak in the distribution is; the width of this peak ($\sim 25^\circ$) corresponds roughly to the mean ℓ -value we are probing with this model, which is around an ℓ of 10. Our 7° beam is shown for comparison. Also witness the symmetry between E and B ; the $\langle U_i U_j \rangle$ portion of \mathbf{S}^E is the same as the $\langle Q_i Q_j \rangle$ portion of \mathbf{S}^B , and vice-versa. All of the $\langle Q_i U_j \rangle$ pieces are identical. This shows the general behavior of the matrix, as all other rows are identical to this row, except shifted such that the peak lies over the pixel in question.

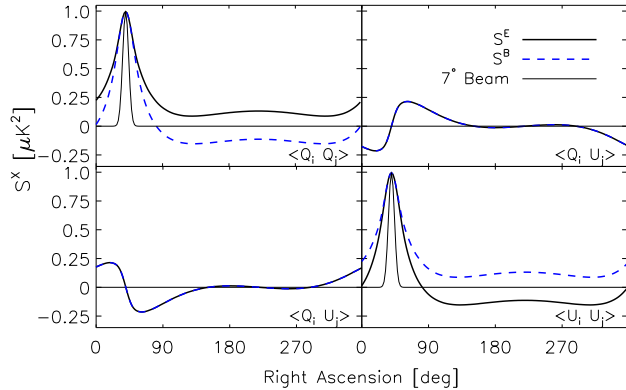


FIG. 12.— Plots of the $ra = 40^\circ$ row of the fundamental signal covariance matrices \mathbf{S}^E and \mathbf{S}^B . The four panels in the plot correspond to the four quadrants of the matrices as labelled. The thick solid line represents \mathbf{S}^E , the thick dashed line represents \mathbf{S}^B , and the thin solid line corresponds to a 7° Gaussian beam for reference.

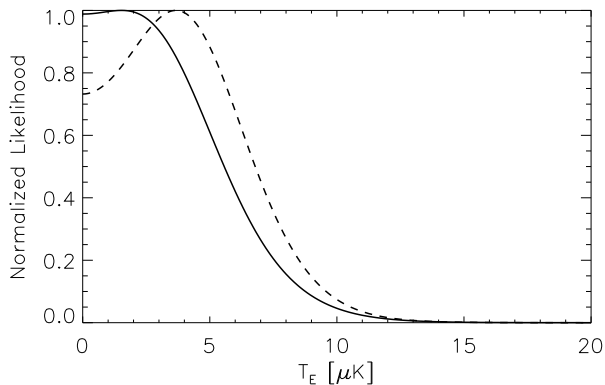


FIG. 13.— Normalized likelihood plot of T_E , with the prior constraint that $T_B = 0$. The solid line is the result for the in-phase channels, and the dashed line is for the quad-phase (null) channels. The resulting upper limit is $T_E < 7.7 \mu K$ at 95% confidence.

5.1.2. Evaluating the Likelihood Function

Now that we have constructed the theory covariance matrix for our parameter space of (T_E, T_B) , we are in a position to calculate the likelihood of our data given this set of models, as defined in Equation (30).

We calculated the likelihood function for all individual and joint channel maps, both for the in-phase and quadrature-phase channels. As reported in K01, all cases were consistent with upper limits. The combined-channel data yield 95% confidence limits of $10.0 \mu K$ on both T_E and T_B . As the B -polarization at large angular scales is assumed to be so much weaker than E -polarization (even taking into account lensing), we can set T_B to be zero. It yields a 95% confidence limit of $T_E < 7.7 \mu K$.

As an interesting side point, we repeated the analysis *without* the offset removal. The corresponding likelihood analysis yields a spurious detection for the in-phase channels at $(T_E, T_B) = (18, 1) \mu K$, while the quadrature channels yield an upper limit of $7 \mu K$ for both T_E and T_B . This gives us a sense of the how well we would have done in the case of no offsets; we see that the offset removal degraded

the upper limit by $\sim 30\%$.

5.1.3. The Co-added Channel Analysis

It is worth noting that the entire mapmaking analysis of §4 can be redone in a slightly different way, where the three channels are combined in the time-ordered data. This technique automatically takes into account any correlations that may be present between the channels. One simply co-adds the time streams with their inverse noise weightings in order to obtain a time stream with the maximum possible signal. Offset removal is still done on the submaps, but since we have combined the channels, a single offset is removed for Q and U for a total of two offsets per section removed, rather than six for the individual-channel analysis.

This was performed for our data, and the corresponding likelihood contours were calculated. The upper limits remained, but were degraded to about $12 \mu K$. This makes sense, considering we subtracted only two offsets per section in this new analysis (as our three channels had been co-added), not six as in the primary analysis. Because the offsets were not perfectly correlated among the three channels, there was residual power left over in the maps due to the imperfect co-addition of the channel offsets; it was this phenomenon that led to the slightly worse upper limits. This result notwithstanding, this analysis is important in that it shows our inter-channel correlations were not a severe problem.

5.2. Limits on Polarization Power Spectra

As discussed in Tegmark & de Oliveira-Costa (2001), CMB anisotropy and polarization is defined by the fields $\{T, Q, U\}$. These quantities can be combined to form six measurable power spectra: TT , EE , BB , TE , TB , and EB . Our analysis of these spectra is presented in de Oliveira-Costa et al. (2002); we give a brief summary of it here.

As POLAR had very weak sensitivity to temperature anisotropy data, we used the COBE-DMR data for the 53 GHz and 90 GHz bands averaged together as discussed in de Oliveira-Costa et al. (2002). We analyzed the spectra in five bands of width $\ell = 5$, but subsequently averaged them into a single band to increase the signal-to-noise ratio. We used the method of quadratic estimators to evaluate the band-powers (see *e.g.* Bond et al. (2000); Tegmark & de Oliveira-Costa (2001)). All band-powers were consistent with upper limits, the results of which are displayed in Table 6.

This technique has the added benefit of explicitly calculating the band-power window functions, while for a maximum likelihood analysis, they are less straightforward to evaluate (Knox 1999). However, there is a new twist on band-powers when it comes to polarization; there is always some amount of leakage into the desired power spectrum from the other five power spectra. In principle, it is possible to choose priors for the quadratic estimators such that fourteen of the fifteen leakages are zero, but the much discussed E - B leakage remains (Tegmark & de Oliveira-Costa 2001), although it can be kept to a minimum at the price of a modest increase in error bars. This leakage is a direct result of “ambiguous” modes existing in the scan strategy; the more ambiguous modes, the worse will be the

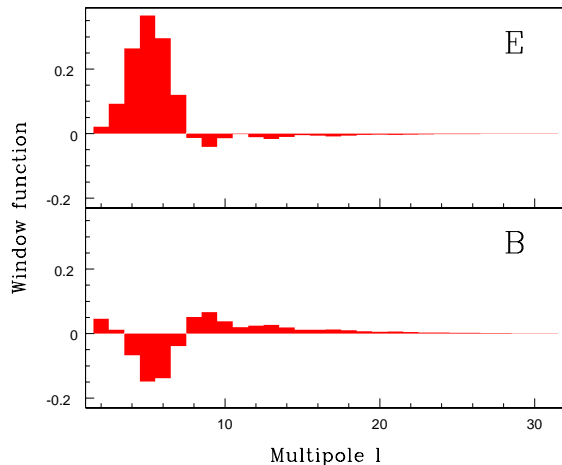


FIG. 14.— The window function for E used to estimate the polarization band-power near $\ell = 5$, shown as a representative example. This shows our sensitivity to E or B for any ℓ -value, when we are aiming in the $2 < \ell < 30$ multipole range. The B window functions are exactly the same as for E (with E and B switched). There is significant leakage of B -power into the E -estimate because of our one-dimensional scan strategy. In general, a scan done over a two-dimensional region with a large sky coverage will have a much better E - B separation and narrower window functions. The width of the window function scales with the inverse of the sky patch size in its narrowest dimension.

leakage (Bunn et al. 2002). Sky coverage that is large, two-dimensional and well-connected will have few ambiguous modes; but the one-dimensional nature of POLAR leads to virtually *all* of the E and B modes being ambiguous.

Figure 14 shows the E window function for a single ℓ -band for $2 < \ell < 8$ for POLAR as an example; the window function was generated using the minimum leakage techniques discussed above. The leakage of B into E is exactly symmetric for E into B , thus we show only the E window function. It is clear that there is a very large leakage from B to E and vice versa. Therefore, the upper limits for E and B cannot be taken separately; we constrain merely the average of the two power spectra.

An early reionization leads to a peak in both the EE auto-correlation and TE cross-correlation spectra at large angular scales Zaldarriaga (1997); Keating et al. (1998). Unfortunately, our EE and TE upper limits are still significantly higher than any possible reionization peak; for $\tau = 0.4$, the concordance model gives $\delta T_{EE} \sim 1.5 \mu K$ and

Table 6 – POLAR-DMR Power Spectrum

	$\ell_{\text{eff}} \pm \delta\ell$	$\delta T^2 \pm \sigma [\mu K^2]$	$\delta T [\mu K]^{(a)}$
T	15.6 ± 6.6	487.0 ± 270.6	$22.1^{+7.4}_{-5.5}$
E	12.6 ± 4.5	-19.7 ± 63.9	$< 6.6(10.4)$
B	12.6 ± 4.5	27.7 ± 63.9	$< 9.6(12.5)$
X	14.0 ± 4.8	-36.7 ± 68.6	$< 5.6(10.0)$
Y	14.0 ± 4.8	-0.2 ± 68.6	$< 8.3(11.7)$
Z	11.4 ± 2.9	-100.0 ± 63.3	$< (5.2)$

^(a) Values in parentheses are $2\text{-}\sigma$ upper limits. Table reproduced from de Oliveira-Costa et al. (2002).

$\delta T_{TE} \sim 4.5 \mu K$, in comparison with our upper limits of $10 \mu K$ on each.

5.3. Constraining Polarized Synchrotron Emission

As discussed in our previous papers (Keating et al. 1998, 2001), synchrotron emission is generally polarized at a level from 10–50% (Brouw & Spoelstra 1976; Davies et al. 1996). Our non-detection of any signal implies that we can place constraints on polarized synchrotron at 30 GHz, but this is not as straightforward as it may seem. As discussed in §3.3.2, we cannot simply extrapolate low frequency polarization measurements such as Brouw and Spoelstra (Brouw & Spoelstra 1976) because of Faraday depolarization. Extrapolation of the unpolarized Haslam 408 MHz data (Haslam et al. 1995) to our frequencies using a spectral index of -3.1 , assuming a polarization fraction of 10%, and smoothing with a 7° beam yields an rms of about $5 \mu K$. Thus, our data favor both a steep spectral index as suggested by recent studies (Platania et al. 1998) and a relatively low polarization fraction at large angular scales.

6. DISCUSSION

At this point, we have apparently learned as much as possible from the POLAR experiment. Given its data set, we have placed limits on CMB polarization power spectra in the context of both a flat band-power model and a concordance model, and we have discussed the lack of substantial synchrotron contamination in our scan region. Let us now ask the questions, could POLAR have done much better? Clearly, more integration time helps, as does increased sensitivity. We showed in §5.1 that the offset removal technique that was required only degraded our limits by $\sim 30\%$, which is not so bad considering that without it, no limits would have been possible.

It is also interesting to ask the question, if we had integrated for a much longer time, and/or our detectors had been much more sensitive, how well could we have actually done in determining E and B on large angular scales? We attempted to answer this question via an additional simulation. We used CMBFast (Seljak & Zaldarriaga 1996) to generate power spectra for a concordance model universe with no B -modes (*i.e.*, only scalar perturbations) and an optical depth to reionization of $\tau = 0.2$; ideally we should recover only E modes from the analysis. We used the HEALPix package (Gorski et al. 1999) to generate twenty sky realizations of Q and U , and observed each with a nearly perfect POLAR, one that had a sensitivity of $0.01 \mu K$ for each of $180 2^\circ$ wide pixels in our $\delta = 43^\circ$ RA strip. We then performed our likelihood analysis on these map realizations limited to our scan region, and found that we “saw” roughly equal amounts of E and B power. This is consistent with the window functions generated in our quadratic estimator analysis of §5.2. On a positive note, we did recover the correct amount of total E and B ; that is, the recovered $C_\ell^E + C_\ell^B$ equaled the initial C_ℓ^E placed in the maps.

Ultimately, POLAR was limited both by its instrument sensitivity and atmospheric limitations to integration time. The atmosphere was also most likely responsible for a time-varying offset. Finally, the one-dimensional scan strategy prevented discrimination between E -modes and B -modes.

Future experiments that effectively deal with these issues may well be able to glean the CMB polarization signals on large angular scales, and hence uncover a wealth of new information with which to increase our understanding of inflation and the details of the Big Bang.

We are grateful to Josh Gundersen, Lloyd Knox, Ed Wollack, Matias Zaldarriaga, Slade Klawikowski, and Phil Farese for many useful conversations. BK and CO were supported by NASA GSRP Fellowships. POLAR's HEMT amplifiers were graciously provided by John Carlstrom. This work has been supported by NSF grants AST 93-18727, AST 98-02851, and AST 00-71213, and NASA grant NAG5-9194.

Press, W. H., Rybicki, G. B., & Hewitt, J. N. 1992, ApJ, 385, 404
 Rybicki, G. B. & Lightman, A. P. 1979, Radiative processes in astrophysics (New York, Wiley-Interscience)
 Rybicki, G. B. & Press, W. H. 1992, ApJ, 398, 169
 Seljak, U. & Zaldarriaga, M. 1996, ApJ, 469, 437
 Sokasian, A., Gawiser, E., & Smoot, G. F. 2001, ApJ, 562, 88, <http://astron.berkeley.edu/wombat/foregrounds/radio.html>
 Stompor, R., Balbi, A., Borrill, J., Ferreira, P. G., Hanany, S., Jaffe, A. H., Lee, A. T., Oh, S., Rabii, B., Richards, P. L., Smoot, G. F., Winant, C. D., & Wu, J. H. P. 2002, Phys. Rev. D, 65
 Tegmark, M. 1997a, ApJ, 480, L87
 Tegmark, M. 1997b, Phys. Rev. D
 Tegmark, M. 1997c, Phys. Rev. D
 Tegmark, M. & de Oliveira-Costa, A. 2001, Phys. Rev. D, 64, 3001
 Turner, M. S. & White, M. 1996, Phys. Rev. D, 53, 6822
 Wright, E. L. 1996, astro-ph/9612006
 Zaldarriaga, M. 1997, Phys. Rev. D, 55, 1822
 Zaldarriaga, M. 1998, ApJ, 503, 1
 Zirin, H., Baumert, B. M., & Hurford, G. J. 1991, ApJ, 370, 779

REFERENCES

- Bennett, C. L., Banday, A. J., Gorski, K. M., Hinshaw, G., Jackson, P., Keegstra, P., Kogut, A., Smoot, G. F., Wilkinson, D. T., & Wright, E. L. 1996, ApJ, 464, L1
 Bond, J. R., Jaffe, A. H., & Knox, L. 1998, Phys. Rev. D, 57, 2117
 Bond, J. R., Jaffe, A. H., & Knox, L. 2000, ApJ, 533, 19
 Brouw, W. & Spoelstra, T. 1976, Astronon. and Astrophys. Supp., 26, 129
 Bunn, E. F. 1993, Ph.D. dissertation, University of California-Berkeley
 Bunn, E. F., Zaldarriaga, M., Tegmark, M., & de Oliveira-Costa, A. 2002, astro-ph/0207338
 Davies, R. D., Watson, R. A., & Gutierrez, C. M. 1996, MNRAS, 278, 925
 de Oliveira-Costa, A., Devlin, M. J., Herbig, T., Miller, A. D., Netterfield, C. B., Page, L. A., & Tegmark, M. 1998, ApJ, 509, L77
 de Oliveira-Costa, A., Tegmark, M., O'Dell, C., Keating, B., Timbie, P., Efstathiou, G., & Smoot, G. 2002, *in preparation*
 Golub, G. H. & Van Loan, C. F. 1996, Matrix Computations, 3rd edn. (Baltimore: Johns Hopkins University Press), 694
 Gorski, K. M., Wandelt, B. D., Hansen, F. K., Hivon, E., & Banday, A. J. 1999, The HEALPix Primer, astro-ph/9905275
 Greve, A., Steppe, H., Graham, D., & Schalinski, C. J. 1994, A&A, 286, 654
 Halverson, N. W., Leitch, E. M., Pryke, C., Kovac, J., Carlstrom, J. E., Holzzapfel, W. L., Dragovan, M., Cartwright, J. K., Mason, B. S., Padin, S., Pearson, T. J., Readhead, A. C. S., & Shepherd, M. C. 2002, ApJ, 568, 38
 Haslam, C., Salter, C., Stoffel, H., & Wilson, W. 1995, NCSA Astronomy Digital Image Library
 Hu, W. 2000, ApJ, 529, 12
 Jansen, D. J. & Gulkis, S. 1992, in NATO ASIC Proc. 359: The Infrared and Submillimetre Sky after COBE, ed. M. Signore & C. Dupraz, Proceedings of the NATO Advanced Study Institute, Les Houches, France, Mar. 20-30, 1991 (Dordrecht:Kluwer)
 Kamionkowski, M. & Kosowsky, A. 1999, Annual Reviews of Nuclear and Particle Science, 49, 77
 Kamionkowski, M., Kosowsky, A., & Stebbins, A. 1997, Phys. Rev. D, 55, 7368
 Kaplinghat, M. et al. 2002
 Keating, B., Timbie, P., Polnarev, A., & Steinberger, J. 1998, ApJ, 495, 580
 Keating, B. G., O'Dell, C. W., de Oliveira-Costa, A., Klawikowski, S., Stebor, N., Piccirillo, L., Tegmark, M., & Timbie, P. T. 2001, ApJ, 560, L1
 Keating, B. G., O'Dell, C. W., Gundersen, J. O., Piccirillo, L., Stebor, N., & Timbie, P. T. 2002, Accepted for publication in ApJ, astro-ph/0111276
 Keihm, S. J. 1983, in Planetary Science Inst. Report
 Kinney, W. H. 1998, Phys. Rev. D, 58, 3506
 Knox, L. 1999, Phys. Rev. D, 60, 103516
 Knox, L. & Song, Y. 2002, Physical Review Letters, 89, 11303
 Kovac, J., Leitch, E. M., Carlstrom, J. E., Pryke, C., Holzzapfel, W. L., & Halverson, N. W. 2002, astro-ph/0209478
 O'Dell, C. W. 2001, Ph.D. dissertation, University of Wisconsin-Madison
 O'Dell, C. W., Swetz, D. S., & Timbie, P. T. 2002, IEEE. Trans. Microwave Theory Tech., 50, 2135
 Platania, P., Bensadoun, M., Bersanelli, M., de Amici, G., Kogut, A., Levin, S., Maino, D., & Smoot, G. F. 1998, ApJ, 505, 473